TÉCNICO LISBOA

Fuel Flexibilization of a Small Scale Low-Swirl Burner for Biogas and Hydrogen

André Silva Justino

Thesis to obtain the Master of Science Degree in

Mechanical Engineering

Supervisors: Prof. Edgar Caetano Fernandes
Eng. Filipe João Marques Quintino

Examination Committee

Chairperson: Prof. Carlos Frederico Neves Bettencourt da Silva
Supervisor: Prof. Edgar Caetano Fernandes
Member of the Committee: Prof. Teodoro José Pereira Trindade

November 2020

To all those who stood by me and helped me continue no matter what. Fall seven times, stand up eight!

Acknowledgments

This work marks a turning point in my academic course, and to an extent in my life. Thus, I would like to leave here my appreciation to all the people who have helped me, one way or the other, along that course.

I'd like to take the opportunity to leave a word of acknowledgement to my orientator Prof. Edgar C. Fernandes and my co-orientator Filipe Quintino, without whom this work wouldn't exist and with whom I have learnt so much. The past months haven't been easy, but they have made me feel welcome and appreciated in the laboratory, and have helped me push the boundaries of my capabilities. To my lab mates, especially Miguel Santos, Bruno Gouveia, and Alexandre Gamboa, with whom I've had the pleasure of sharing a workspace where I felt I belonged.

To all the colleagues and friends who I have met over the years and who have turned my time at school and university from a chore to an absolute pleasure, particularly Rui Fonseca, Gabriela Sousa, Duarte Madeira, João Nabais and António Pacheco, and many, many others who have both laughed with me and held out a hand in the times I needed it the most.

To my family, who have seen me grow to who I am today, and especially to my mom and dad, who have held me ever since I was born and continue to do so every time I need it. To my grandparents, who seem to be an endless source of wisdom, and to my uncles and aunts. They have helped me become who I am today and will forever be with me. To my sister Sara, who constantly reminds me why I should strive to be the best I can be. And finally, to Lee Hye Rin, who always puts a smile on my face, no matter how gloomy everything else is.

To each and every one, thank you. I wouldn't have done it without you.

This work was developed at the Thermofluids, Combustion and Energy Systems laboratory of the IN+ - Center for Innovation, Technology and Policy Research.

Resumo

As atuais preocupações ambientais têm levado a maiores restrições de emissões e a uma maior procura de métodos capazes de conseguir baixos níveis de emissões e de incorporar combustíveis mais ecológicos, como o biogás. Estes devem, idealmente, ser capazes de estabilizar chamas mais pobres, com o objetivo de reduzir as emissões de NO_x.

O desenvolvimento das chamas em swirl, um desenho baseado na adição de rotação ao escoamento, vem sendo aperfeiçoado há décadas, e originou o queimador de low-swirl (LSB, Low-swirl burner). Apesar de terem sido feitos vários estudos acerca da escalabilidade e adaptabilidade a novos combustíveis, a maioria dos trabalhos utilizou queimadores de maior potência e maiores dimensões.

Este trabalho pondera a possibilidade de usar um queimador menor e avalia os limites de estabilidade para diversas composições de combustíveis com biogás e hidrogénio. Os testes mostraram que chamas enriquecidas com hidrogénio exibem blow-off a razões de equivalência menores que chamas de metano, baixando-se o limite de uma gama de 0.75 a 0.85 para 0.6 a 0.7. Além disso, mostrou-se que as anteriores são menos afetadas pela adição de CO_2 que estas últimas, permitindo uma queima abaixo de $\phi = 0.6$.

Ademais, estimativas de emissões para chamas ideais mostraram uma quebra nos níveis de emissões de NO_x para condições pobres. Estimou-se uma redução das emissões em cerca de 80% numa redução de ϕ de 1 para 0.8, e uma redução adicional para metade para um combustível base de 60/40% de CH_4 e CO_2. A adição de hidrogénio não mostrou um impacto significativo nas emissões.

Palavras-chave: Low-Swirl, Biogás, Hidrogénio

Abstract

The current environmental concerns have led to increased restrictions on emissions and a higher demand of methods capable of achieving both lower pollutant emission levels and incorporating environmentally friendly fuels such as biogas. These should ideally be able to stabilize flames under leaner conditions, with the goal of lowering the NO_x emission levels.

Development of swirled flames, a design based on adding rotation to the flow, has been ongoing for decades, and has eventuated the low-swirl burner (LSB) design. Although several studies have been made on the scalability and fuel flexibility of the design, most previous work has focused on higher thermal loads and larger burners.

This study ponders the possibility of using a smaller burner and evaluates the stability limits for different compositions of biogas and hydrogen as fuel. Tests showed that hydrogen-enriched flames exhibited blow-off at lower equivalence ratios than methane flames, lowering the lean blow-off limit from a range of 0.75 to 0.85 to values of 0.6 to 0.7. In addition, it was shown the former are less affected by the addition of CO_2 than the latter, allowing for burning at equivalence ratios under 0.6.

Furthermore, emissions estimates for ideal flames showed a drop in NO_x levels for leaner conditions. A drop from a ϕ of 1 to 0.8 was estimated to drop NO_x emissions by roughly 80%, and emissions drop even further to about half for a base fuel with a 60/40% split of CH_4 and CO_2. Hydrogen addition in the fuel was shown not to significantly impact emissions.

Keywords: Low-Swirl Burner, Biogas, Hydrogen

Contents

List of Tables

List of Figures

Nomenclature

Acronyms

AC	Alternating Current.
AD	Anaerobic Digestion.
BG	Biogas.
HSB	High-Swirl Burner.
IA	PIV Interrogation Areas.
LHV	Lower Heating Value (per mol).
$\overline{LHV}$	Lower Heating Value (per kg).
LPM	Liters Per Minute.
LSB	Low-Swirl Burner.
MW	Molar Weight/Molar Mass.
PIV	Particle Image Velocimetry.
RFZ	Reverse Flow Zone.
SLPM	Standard Liters Per Minute.

Chemical Species

C_2	Diatomic carbon.
CH_4	Methane.
CH	Methylidyne radical.
CO_2	Carbon dioxide.
CO	Carbon monoxide.
H_2O	Water.
H_2	Hydrogen.

N_2 Nitrogen.

NO_2 Nitrogen dioxide.

NO Nitric oxide.

O_2 Oxygen.

NO_x Nitrogen oxides, NO + NO_2.

Greek symbols

α Angle swirler vanes.

μ Dynamic viscosity.

ν Kinematic viscosity.

ϕ Fuel-air mixture equivalence ratio.

ρ Density.

Roman symbols

$\dot{m}$ Mass flow rate.

$\dot{n}$ Molar flow rate.

$\dot{V}$ Volume flow rate.

a_x Normalized flow divergence rate.

C_p Constant pressure specific heat.

D Diameter of burner.

e_x Error of x in percentage.

G Axial flow of momentum.

G' Modified axial flow of momentum.

L_i Swirler recess.

p Pressure.

R_0 Universal gas constant.

R_b Burner radius.

R_h Radius of the centre hub.

Re Reynolds number.

S Modified swirl number.

S_0 Swirl number.

S_L Laminar flame speed.

S_T Turbulent flame speed.

T Temperature.

u' Turbulent velocity fluctuations.

U_∞ Bulk flow velocity.

U_a Outer annulus bulk flow velocity.

U_c Center bulk flow velocity.

U_x Uncertainty associated with x.

x_0 Virtual flow origin.

x_f Flame brush position.

y_x Molar fraction of species x.

U, V, W Velocity Cyllindrical components.

x, r, θ Cyllindrical coordinates.

x, y Cartesian coordinates.

Subscripts

$0, n, k$ Computational indexes.

ad Adiabatic.

f Fuel.

max Maximum.

sp Set Point.

vent Ventilator.

Chapter 1

Introduction

1.1 Motivation

The current necessity for energy and power as a pillar for the development of world societies has led to an incessant increase in energy production demands [1], which for centuries has been largely met using fossil fuels. This practice has led to a number of environmental problems, among which the decrease of air quality due to the increase in air pollutants, particularly in urbanized centres, leading to a number of consequences ranging from an increase in catastrophic meteorological events to numerous impacts on human health, such as a number of acute and chronic diseases and even reduced life expectancy due to premature mortality, as well as significant damage to the Earth's ecosystems, impacting all living beings [2].

Although combustion has been a staple of energy generation for centuries, this backdrop has urged a development of cleaner alternative methods, which have gradually reduced the necessity for the usage of combustion, especially in smaller applications. However, due to a large amplitude of output capacity of these methods, often rather inconsistent by themselves, a need for combustion based power generation is still very much present albeit with ever stricter restrictions, especially on emissions levels [3]. This has led designers of combustion based systems to adapt. New power generation solutions have been developed, capable of not only reducing pollutant emissions but also allowing the possibility of using alternative fuels sourced in such way that a steady supply can be provided indefinitely, ideally causing very little or no harm to the surroundings.

The usage of biogas yields an even more optimistic outlook, as it can typically be sourced from Anaerobic Digestion (AD), a process which consists of the decomposition of organic substrates within an oxygen-free environment, meaning the solution would yield energy from biodegradable waste, a source which would not be utilized and possibly neglected [4, 5]. Furthermore, it's often a by-product of agriculture and animal husbandry, meaning it would be promptly available in rural regions where these are carried out and infrastructure may be lacking, and it would be comparatively inexpensive, especially if implemented in large scale. Despite these advantages, biogas is considered to be a poor fuel largely due to the CO_2 within its composition, especially when compared to most carbohydrates such as propane

and methane (which constitutes a large part of biogas in the first place) [6, 7], as carbon dioxide is not consumed in an ideal reaction, meaning no power is added by the addition of CO_2. However, due to its large heat capacity, the thermal inertia of the mixture is increased, leading to a lower flame temperature, and the increased diffusion caused by a higher component of CO_2 slows the reaction kinetics, which causes blow-off to occur at higher equivalence ratios.

An important focus of reducing pollutant emissions is centred around reducing the levels of NO_x, which can be achieved by burning at lower equivalence ratios (ϕ), closer to the lean limit, since one of the main formation reactions for stoichiometric NO_x is a thermal process (Zeldovich Mechanism) [8]. This, in turn, poses some challenges. Leaner flames tend to become less stable as they approach the stability limit, causing, among others, oscillations, noise and possibly flame blowout. This stability problem is aggravated by the aforementioned poor properties of biogas. A number of processes have been suggested and developed to improve the properties of biogas, such as scrubbing, or amine gas treating. The goal in these methods is to remove the undesirable by-products of anaerobic digestion, like H_2S and CO_2, increasing the methane component in the fuel, and thus improving its properties [5]. These methods, however, require specific (and often expensive) equipment, which would negate the economic and accessibility advantages of using biogas.

Alternatively, the enrichment of biogas can be a good solution to achieve the same goal by adding a fuel which can mitigate the negative effects of carbon dioxide. Typically, methane enrichment is used, yielding a similar result to the aforementioned processes. However, hydrogen (H_2) has emerged as a prime candidate for this usage, as its combustion properties contrast even further with the Biogas'. While Biogas has a lower flame speed, and higher lean stability limits, H_2 is notable for its high combustion rate, and in consequence its elevated flame speed, as well as its low lean combustion limits, properties which are desirable when burning biogas.

These differences in fuel properties comprise a fascinating challenge in adapting and attuning the available technologies to the contemporary requirements, so as to continue the usage of combustion not as a burden, but as a solution to the environmental problem.

1.2 Swirl Burners

Swirl stabilized flames were first introduced in the mid 1960's as a technique of flame stabilization mainly for large applications, usually non-premixed, using the basic principle of adding a tangential component to an outer annulus of the burner exit flow. This is usually achieved in one of two ways: either by way of guide vanes or by injecting air tangentially into the main flow of premixed fuel [9]. In the original high swirl designs, the burner often contained a cylindrically shaped hub on the outlet, with a small orifice from where fuel was injected onto the flow, and which created a low pressure zone where the flow would display recirculation. This zone, fittingly named the Reverse-flow Zone (RFZ), created stagnation points where the flame could anchor as well as promoting mixing of the fuel and air and increasing the residence time, keeping the hot reaction products in this zone, thereby preventing quenching and sternly reducing the possibility of blow-off [10]. Due to the high level of turbulence of the High-Swirl Burner (HSB) design,

flames for these burners were usually rich, as lean flames tend to destabilize much more easily.

This technique was later enhanced by Chan et al. in the early 1990's [11], modifying the original design by changing the flame to a premixed flame and introducing a centre non-swirled channel. This drastically altered the flame structure as it was now designed to stabilize a detached flame through the flow divergence downstream of the outlet, exploring the propagating nature of the premixed flame instead of relying on recirculation of the flow in order to anchor the flame, which, due to the premixed condition of the flame, was no longer necessary for fuel mixing. This new design was initially executed by adding a tangential air flow upstream of the burner outlet, but was later remodelled as it was deemed too complicated for widespread use. A small piece, called a swirler, was then developed to be placed where the tangential inlet would be [12], dividing the flow into two sections: a central non-swirled section, restricted by a perforated plate in order to induce a drop in pressure, and an outer swirled section, where a tangential component is introduced onto the flow through a set of angled vanes. A number of modifications have been proposed through the years, changing swirler, flow and even ambient conditions [13–15], through which this design proved its adaptability by keeping a largely similar flowfield and flame shape in these conditions, provided certain criteria, which will be presented in Section 2.1.1, are met. Low-swirl burners (LSB) have been shown to be capable of operating with loads as low as less than 1 kW for households and as high as 7.5 MW for industrial applications, burner diameters varying from 12 mm to 254 mm, and have shown promising results utilizing methane, syngas (a mixture of CH_4 and CO), hydrogen and various mixtures of fuels [14, 16, 17].

More importantly, the LSB design has reliably allowed for the stabilization of lean flames at lower equivalence ratios and temperatures, therefore reducing the emissions levels of such pollutants, particularly the aforementioned NOx. Very low levels of under 5 ppm are possible under the leanest conditions, a significant improvement over the common high-swirl burner (HSB) design, as previous works have been able to stabilize a methane flame at equivalence ratios as low as $\phi = 0.5$ [17].

1.3 Objectives

The goal of this work is to investigate the effect of lean biogas combustion and hydrogen enrichment in small scale low-swirl burners, comparing flame geometry and stability limits for various compositions. Albeit the LSB design has been studied for use with hydrogen-enriched syngas, most studies employ a higher load burner, usually of a larger diameter so as to keep the bulk flow velocities within the same order of magnitude as the flame speed (in this case, the turbulent flame speed, S_T). Hence, the main goal can be sub-divided into 3 main goals:

1. The acquisition of non-reacting flow parameters, and subsequent validation and quantification of the low-swirl flow field through Particle Image Velocimetry acquisitions;

2. The definition of stability limits for a number of fuel scenarios, and comparison of the effects of fuel compositions on them.

3. The estimation of the emissions in the ideal lean scenarios, and hypothesizing of the ultra low NO_x

claim for the LSB design.

1.4 Thesis Outline

This work is divided into five main sections: Introduction, Background, Implementation, Results and finally, Conclusion. On a first instance, the basic principles of swirl burning and the consequent adaptation to low-swirl burning are presented, and the objectives of the work are defined. A theoretical background for swirl burning is then described, as well as properties of the fuels to be used, particularly methane (CH_4), carbon dioxide (CO_2) and hydrogen (H_2).

A thorough description of the experimental setup for both the particle image velocimetry (PIV) and image capture tests, as well as an explanation of the processing undertaken to obtain the results. Test conditions for the fuels are also defined in this section.

Results are presented firstly for the non-reacting flow, defining the flow field for different ventilator velocities, both in an axial/radial plane and in a radial/tangential plane. Using these results, it was possible to define the flow characteristics for the different velocities. Flame images are also presented for an array of fuel conditions, showing the effect on flame shape and position. Blow-off limits for the same fuel conditions were then defined, and emission results were estimated for ideal conditions. Finally, the Conclusions section presents the interpretation of the obtained results, and suggests future testing to be undertaken on this subject.

Chapter 2

Background

2.1 Theoretical Overview

The swirl burner design is a historical design for flame stabilization, finding its way into diverse industrial applications such as turbines and boilers, and providing an economical and reliable form of flame stabilization. The basic principle of swirl combustion is the introduction of a tangential component of velocity onto the burner outlet flow, causing a spiralling flow which, in its original diffusion flame design, caused an increase in divergence of the flow, and increased the rate of entrapment through way of recirculation. This allowed for better mixing between the swirling air and the fuel, often injected as a central gas or atomized particle flow [9, 10].

In any swirl burner, the initial challenge is to quantify a value to characterize the type and characteristics of the flow, and consequently of the flame. This dimensionless ratio, first proposed by Chigier and Beér [18], is called the Swirl Number S_0, and it represents a ratio between the axial fluxes of tangential and axial momenta, made non-dimensional by the burner radius, being represented as follows:

$$S_0 = \frac{G_\theta}{G_x R_b} \tag{2.1}$$

where G_θ is the axial flux of tangential momentum (kg m^2 s^{-2}), G_x refers to the axial flux of axial momentum (kg m s^{-2}), and R_b is the burner radius (m). A cylindrical coordinates system (x, r, θ) is considered for the axial, radial and tangential directions, respectively, with the dimensions in m, and the velocities (U, V, W) represent the velocities for each respective dimension (m s^{-1}). Should it be assumed that the flow is perfectly axisymmetric along the x axis, the fluxes of momentum are then defined by:

$$G_\theta = \int_0^{R_b} (Wr)\rho U 2\pi r dr \tag{2.2a}$$

$$G_x = \int_0^{R_b} 2\pi r \rho U^2 dr + \int_0^{R} 2\pi r p dr \tag{2.2b}$$

where ρ is the local density of the flow (kg m^{-3}) and p refers to the static pressure (Pa).

The latter, however, is somewhat difficult to measure in an experimental apparatus as it requires

various measurements of static pressure within the flow, possibly disrupting it. Thus, an alternative definition of the swirl number G'_x was established, substituting the contribution of the static pressure by an approximation using the tangential velocity [19], yielding:

$$G'_x = \int_0^{R_b} 2\pi r \rho \left(U^2 - \frac{1}{2} W^2 \right) dr \tag{2.3}$$

and resulting in a modified swirl number, hereby referred to as S, which, if constant density was to be assumed in the whole control volume, can be defined as:

$$S = \frac{G_\theta}{G'_x R_b} = \frac{\int_0^{R_b} r^2 U W dr}{R_b \int_0^{R_b} r \left(U^2 - \frac{1}{2} W^2 \right) dr} \tag{2.4}$$

This swirl number is fundamental to distinguish between low swirl and high swirl applications. A boundary was set at S equal to 0.6, above which the flow would be considered a high swirl flow, and below, a low swirl flow. These low swirl flows showed relatively low flow divergence, which resulted in a much smaller recirculation zone, and showed worse results that the higher swirl flows for a typical high swirl burner geometry. They were therefore considered undesirable for widespread use [9, 10].

In addition to S, the Reynolds number of the flow is also important to define its characteristics, as turbulence level is crucial to the turbulent burning velocity S_T. For the flow on the outlet of swirl burners, Re can be defined as:

$$Re = \frac{U_\infty D}{\nu} \tag{2.5}$$

Where U_∞ corresponds to the bulk flow velocity (m s^{-1}), calculated by averaging the flow velocity for the outlet surface, D is the burner diameter (m), or two times R_b, and ν represents the kinematic viscosity of the fluid, in this case, air (m^2 s^{-1}).

It was observed that within the swirl conditions, four main types of flow were observable [20], as shown in figure 2.1:

1. Type 1 flows exhibited an annular recirculation zone, inside of which the flow would not show any recirculation. These would be present in high velocity flows and would generate long detached flames due to low entrapment of combustion reactants.

2. Type 2 flows would be present in lower velocity burners, and would generate a closed ovate shape which would restrain the reactants and generate short, high intensity flames, either detached or attached.

3. Type 3 flows describe a situation between types 1 and 2, as the centre flow is of high enough velocity to partially penetrate the type 2 "bubble", but not enough to fully traverse it, thereby following a radial trajectory.

4. Type 0 flames were defined as a swirling flame which showed no recirculation zone.

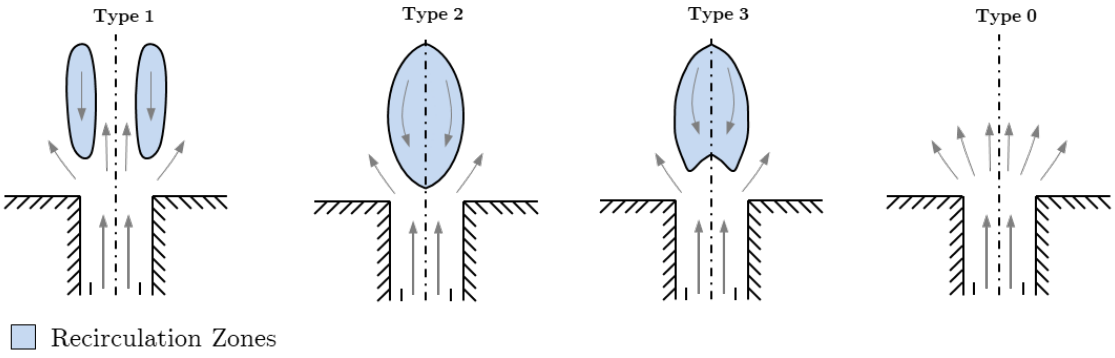

Figure 2.1: Types of swirling flows, with defined recirculation zones. The arrows show the flow in an axial/radial plane, perpendicular to the burner outlet.

2.1.1 Low Swirl Burners

Initially, type 0 flames were regarded as undesirable, as they showed poor performance for flame stabilization in a typical high-swirl layout, which relies on flow recirculation for the mixing of fuel and air, and the resulting stagnation points for anchoring the flame, and preventing blow-off.

However, in 1992, utilizing a novelty burner with no inner hub, of S in the region of 0.05-0.3, Chan et al. stabilized a detached premixed flame not through recirculation, but rather through the divergence of the flow as it exited the burner nozzle [11]. This design made use of the propagating nature of premixed flames and, due to deceleration of the flow, the flame would rest at a location where the flow velocity matched the local flame speed, creating a slight cup-like shape due to the increased mass flow (and corresponding velocity) in the outer region of the flow, and the lower velocity of the undisturbed centre region. Despite this light curvature, the flame showed properties resembling an ideal 1D combustion layout. Initial results were already promising for the LSB geometry as a stabilization method for premixed lean flames, since the initial design was capable of stabilizing a methane flame within the $0.8 < \phi < 1$ range. These results first showed the potential of the LSB for lean low emissions burning. The layout of this burner used air inlets from where air would be injected tangentially into the flow, generating swirl in the outermost zone of the burner flow. This method, however, required a dedicated burner design, as well as a second air supply system, negating some advantages which were attributed to it, especially the adaptability to smaller applications.

To solve this issue, Yegian et al. [12] developed a novel solution to generate the desired flow conditions, creating a piece which was divided into a central partial blockage of the flow aimed at causing a pressure loss, and consequent reduction of velocity, while still not generating undesired recirculation, and an outer annular section composed of guide vanes which introduced the swirling motion onto the flow. This led to the development of a simplified swirl number calculation, based on the geometric parameters of this piece.

$$S = \frac{2}{3}\tan\alpha \frac{1-(R_h/R_b)^3}{1+(R_h/R_b)^2\left((U_c/U_a)^2-1\right)} \tag{2.6}$$

where α is the vane angle, R_h is the radius of the non-swirled centre hub (m), R_b is the burner outer

radius (m), with U_c referring to the bulk velocity for the central section $[0, R_h]$, and U_a to the bulk axial velocity in the swirled annulus $[R_h, R_b]$. Both flow bulk velocities are calculated by averaging the velocity in each respective section, dividing the flow rate by the cross-sectional area at the burner outlet, yielding a velocity result (m s^{-1}).

This piece, called the swirler, is the fundamental piece of the current LSB design, as it is the piece responsible for generating the according flow field, and it's much cheaper, scalable and easy to produce than the previous implementation. Further studies on swirler geometry have been made, from which a number of conclusions can be taken. An increase in swirl number, either by increasing the angle of the vanes or decreasing the hub radius, will cause the flame to move upstream, and in extreme cases can cause significant recirculation and possible flame anchoring on the burner outlet, as the flame nears the high swirl condition. An increase in screen blockage yields a similar outcome, as it also increases the swirl number [13]. The swirler used in this work, and a more detailed analysis of its specifications is present in Section 3.2.

Fuel Adaptability

Extensive studies have been conducted on the fuel flexibility of the LSB setup, which have shown a broad acceptability range of fuels, particularly hydrocarbons [17]. This flexibility to the variation in fuel composition can be explained by the equilibrium equation for the velocity balance at the flame front [14]:

$$1 - \frac{dU}{dx}\frac{x_f - x_0}{U_\infty} = \frac{S_T}{U_\infty} = \frac{S_L}{U_\infty} + \frac{Ku'}{U_\infty} \tag{2.7}$$

In this equation, U and U_∞ are the aforementioned axial velocity and bulk axial velocity, respectively, x_f represents the flame front coordinate in m, x_0 is a virtual origin of the flow, the point where velocity U is equal to the flow bulk velocity U_∞, also in m, K is an non-dimensional specific constant of the fuel (although it should be noted that it represents an approximation, as turbulent flame speed tends to experience an effect of "bending" and stagnate for higher turbulence levels [21], and u' is the root mean square (RMS) of the turbulent velocity fluctuations (m s^{-1}).

This equation, which applies for all self-similar LSB setups, approximates the divergence of the flow linearly, with a constant divergence ratio $a_x = (dU/dx)/U_\infty$ and represents the turbulent flame speed as a function of the turbulence intensity, with the added factor of the linear flame speed. This equation is applied on the centreline of the flow, where the flame is expected to have its closest point to the burner, and where turbulence is generated by the central screen of the swirler. Littlejohn et al. [22] refers the turbulence intensity generated by the screen is proportional to the bulk velocity, which would mean the main factor for the flame brush position is the normalized laminar flame velocity S_L/U_∞. For most hydrocarbons, the laminar flame velocity does not vary significantly, and the flame brush position should not differ for most hydrocarbons, which holds especially true if the bulk velocity is significantly greater than the linear flame speed S_L.

Although this helps explain the adaptability of the LSB for hydrocarbons, it poses problems for a fuel like hydrogen, for which the flame speed is significantly greater. Tests for the addition of H_2 to

hydrocarbons showed the LSB could operate up to 100% H_2, albeit this condition significantly altered the flame shape, as due to the increased flame speed, the flame anchored on the burner outlet. Nevertheless, the regular LSB stabilization mechanism remains unchanged until 60% H_2 [23], and the addition of hydrogen lowered the blow-off limit of the flames [15, 17]

Scalability

As mentioned previously, the LSB design shows excellent scalability properties. Burners with varied power outputs, as low as 1 kW and as high as 10 MW, have shown consistent stability and emissions results, which has allowed the design to be established as a viable commercial solution for industrial applications, such as heaters and boilers.

This has led most research work to favour higher power, larger systems, as a demand was present for burners capable of meeting the stringent pollutant thresholds reliably. Thus, several results have showed the capabilities of the LSB, both at atmospheric and in boiler conditions [15, 24], for a variety of fuels.

Despite this, more recent studies for smaller burners, particularly a burner of the same dimensions as the one used for the laboratory tests (D = 25.4 mm), show similar trends of divergence as the bigger LSB setups [16], indicating flow field coherence, and the same basic principles as the larger, more thoroughly studied systems.

2.2 Fuel Properties

For the laboratory tests, the main goal was to verify the LSB's adaptability to varied fuels, under various combustion regimes, particularly the combustion of biogas and the viability of its mixing with hydrogen. Both these fuels constitute attractive alternatives to the common fuels used for combustion, for different reasons.

Biogas is a biofuel which can be sourced naturally through Anaerobic Digestion of organic matter, and is mainly composed of methane (CH_4) and carbon dioxide (CO_2), also containing traces of other species such as N_2 and residual amounts of H_2, O_2 and CO, among others [5]. Although its renewable origin is one of its merits, the wide variation of its components poses challenges for the design of a burner system, as it has been shown that due to the inert nature of the carbon dioxide, it is not consumed in a reaction. However, due to its relatively high specific heat, the thermal inertia of the fuel increases, which reduces flame stability and burning speed [6, 25]. For these studies, biogas was simulated by creating two combinations of methane and carbon dioxide, with 60% and 80% CH_4 by volume.

Hydrogen, on the other hand, has very good combustion properties, and it has been proven to improve the lean stability of methane-air and syngas flames [17]. Its high burning rate and high mass heating value, combined with the fact that, in a perfect setting, the only byproduct of its combustion is water (H_2O), make it an attractive fuel option, and it has been show to increase efficiency and lower irreversibilities in a variety of applications [26]. However, its increased flame speed and reactivity can lead to a faster combustion, which in turn can lead to flashback if the burner conditions are not ideal, and the increased flame temperature of hydrogen may lead to higher emission levels for comparable equivalence ratios.

Thus, it is important to define the properties of the reacting fuels used in the tests. The properties presented are molecular weight (MW), density (ρ), lower heating value (LHV), both molar and per unit of mass, the adiabatic temperature of combustion and the flame speed.

Table 2.1: Combustion properties of methane and hydrogen at 25°C and 1 atm. [27, 28]

Fuel	MW [kg kmol^{-1}]	ρ [kg m^{-3}]	LHV [MJ kmol^{-1}]	$\overline{LHV}$ [MJ kg^{-1}]	T_{ad} [K]	S_L $(at\ \phi = 1)$ [m s^{-1}]
Methane (CH_4)	16.043	0.6565	802.41	50.0	2226	0.36
Hydrogen (H_2)	2.016	0.082	241.92	120.0	2527	2.1

These properties then enabled the calculation of important parameters to the flow, such as the equivalence ratio ϕ, which is defined by the ratio between the amounts of air and fuel supplied to the burner and the stoichiometric air fuel ratio, as shown:

$$\phi = \frac{\left(\frac{A}{F}\right)_{st}}{\left(\frac{A}{F}\right)} \tag{2.8}$$

The stoichiometric air fuel ratio is defined as the amount of air necessary to completely oxidize the fuel divided by the amount of fuel itself. Note that both a mass air/fuel ratio and a molar air/fuel ratio can be defined, depending on whether mass or molar values are used in the equation. However, provided the units used are consistent, the stoichiometric ratio ϕ is independent of whether molar or mass ratios are used, and the equation holds true for both cases. In the case of the LSB, the main goal is to achieve lower emissions when burning, an therefore lean conditions ($\phi < 1$) are favoured, as will be shown in Section 4.4.

The calculation of the flame power was made with the following equations, combined with the ideal gas law:

$$P = \dot{m}_f \overline{LHV} = \dot{n}_f LHV = \frac{p\dot{V}_f LHV}{R_0 T} \tag{2.9}$$

Other Gas Properties

Knowing the combustion properties of the reacting fuels, it is also important to define the properties of the other reacting substances. Since these gases are not considered to be reacting fuels by themselves, there are evidently no values relating to combustion, but it is still relevant to define the thermal and fluid properties, such as the heat capacity C_p, the density ρ, and the viscosity μ. From the latter two, the kinematic viscosity ν can be calculated:

Table 2.2: Properties of air and CO_2 at 25°C and 1 atm [27, 29]

Gas	MW [kg kmol^{-1}]	ρ [kg m^{-3}]	C_p [kJ kmol^{-1} K^{-1}]	$\mu \times 10^6$ [N s m^{-2}]	$\nu \times 10^6$ [m^2 s^{-1}]
Air	28.96	1.203	29.163	18	15.41
CO_2	44.01	1.825	37.198	14.8	8.11

Using the obtained values from tables 2.1 and 2.2, the properties for each simulated composition of fuel can be obtained:

Table 2.3: Properties of the simulated mixtures of methane, biogas and hydrogen for testing.

Biogas Composition	Hydrogen Percentage	MW [kg kmol^{-1}]	ρ [kg m^{-3}]	LHV [MJ kmol^{-1}]	$\overline{LHV}$ [MJ kg^{-1}]
Methane	0 %	16.043	0.6565	802.41	50
	10 %	14.640	0.5991	746.36	50.98
	20 %	13.238	0.5416	690.31	52.15
	30 %	11.835	0.4842	634.26	53.59
BG 80/20	0 %	21.636	0.8902	641.93	29.67
	10 %	19.674	0.8094	601.93	30.60
	20 %	17.712	0.7286	561.93	31.73
	30 %	15.750	0.6477	521.93	33.14
BG 60/40	0 %	27.230	1.1239	481.45	17.68
	10 %	24.708	1.0197	457.49	18.52
	20 %	22.187	0.9155	433.54	19.54
	30 %	19.666	0.8113	409.59	20.83

Chapter 3

Implementation

In the laboratory tests, there are necessary assumptions that must be made in order to fill in unknowns which are not practical or simply impossible to measure. For these tests, the following were considered:

1. The environment was considered to be at standard pressure and temperature conditions;
2. The non-reacting flow was considered to be incompressible, making air density ρ constant in the entire control volume;
3. All fuels were perfectly mixed in the mixing chamber, and the final fuel composition is perfectly uniform;
4. The fuel is ideally premixed with the air inside the burner end, and ϕ is considered to be uniform as it exits the burner.

3.1 Experimental Setup

3.1.1 Burner Setup

For the performance tests, an open flame LSB setup was assembled in the laboratory, as depicted in Figure 3.1. This setup was conceived to be modular and easily modifiable, not just in height and location relative to the supporting structure, but also in orientation, as was necessary for the PIV measurements parallel to the burner outlet.

Air flow was provided by a ventilator controlled by an AC power supply, which was in turn attached to a Fluke 123 Series scopemeter (min. division 0.1 V), with the aim of obtaining a more accurate reading of the voltage supplied to the ventilator. Although the power supply was capable of an output of up to 240V, the ventilator had an inbuilt safety feature which restricted the voltage to roughly 180V, shutting off should the input exceed this value. This limited tests to a maximum air flow rate of just over 150 litres per minute (LPM), which translates to a maximum Reynolds number (calculated as per Section 2.1) of approximately 8500, limiting the possibilities of finding the blow-off conditions of higher power output flames, or even stabilizing them at the desired lean conditions.

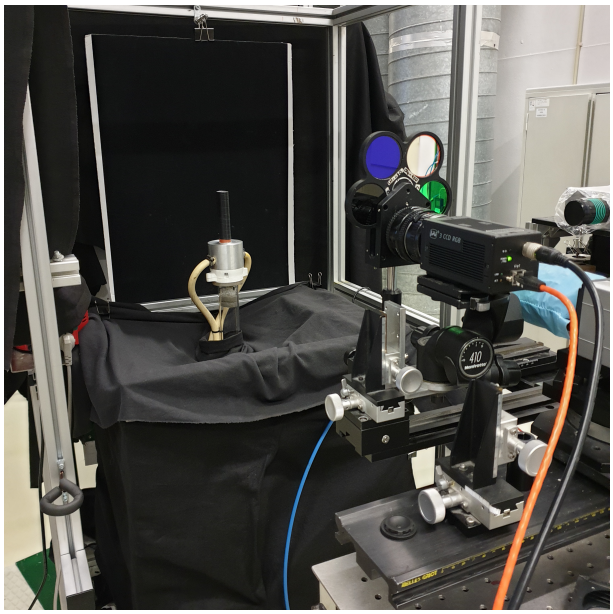

Figure 3.1: Setup for photo analysis. The JAI camera can be seen on the right foreground, attached to the lens and behind the bandwidth filters, the burner end on the left background.

The ventilator was linked to a settling chamber, 50 cm long and 42 mm in internal diameter, encompassing three layers of pressure drops so as to stabilize the flow. The burner was then assembled on the end of this chamber through a custom-made quick release adapter, which allowed for the easy removal of the burner end. This cylindrical burner end constricts the flow to the diameter of 1 inch (2.54 cm), and it maintains a cylindrical geometry until the burner outlet. The swirler was placed upstream of the outlet, at a recess distance L_i of 1 inch, or $2R_b$. The geometry of this swirler piece, as well as its placement within the burner will be further discussed in Section 3.2.

Also within this burner end were the fuel inlets, meaning the air/fuel mixture was formed at this point. Methane, hydrogen and carbon dioxide were bottle sourced (Air Liquide Alphagaz bottles, $>$99.95% purity), while the propane used in earlier testing was pipe sourced. All gases were measured through a set of Alicat M-Series digital flow meters of varying capacities, ranging from 5 SLPM to 50 SLPM. SLPM indicates standard litres per minute, a flow measurement unit that makes use of the flowmeter's inbuilt thermometer to provide a constant mass flow under all conditions. Although the standard definition refers to the equivalent mass of a litre per minute of gas at 1 bar and 0° C, Alicat defines SLPM as the mass of a litre per minute at ambient conditions (1 atm and 25°).

In particular, biogas mixtures with higher percentage of carbon dioxide required a larger flow of CO_2 to be supplied, and therefore a 50 SLPM capacity flow meter was employed. A 20 SLPM capacity flow meter was used for the control of CH_4 flow rate, and two separate 5 SLPM flow meters were used for CH_4. All flow meters were controlled using the LabView software, and were connected to a mixing chamber, which in turn was connected to the fuel inlets of the burner. Propane, on the other hand, was not mixed with any other gases and bypassed the mixing chamber, being sourced directly from an Alicat flow meter of 5 SLPM capacity to the burner's fuel inlets.

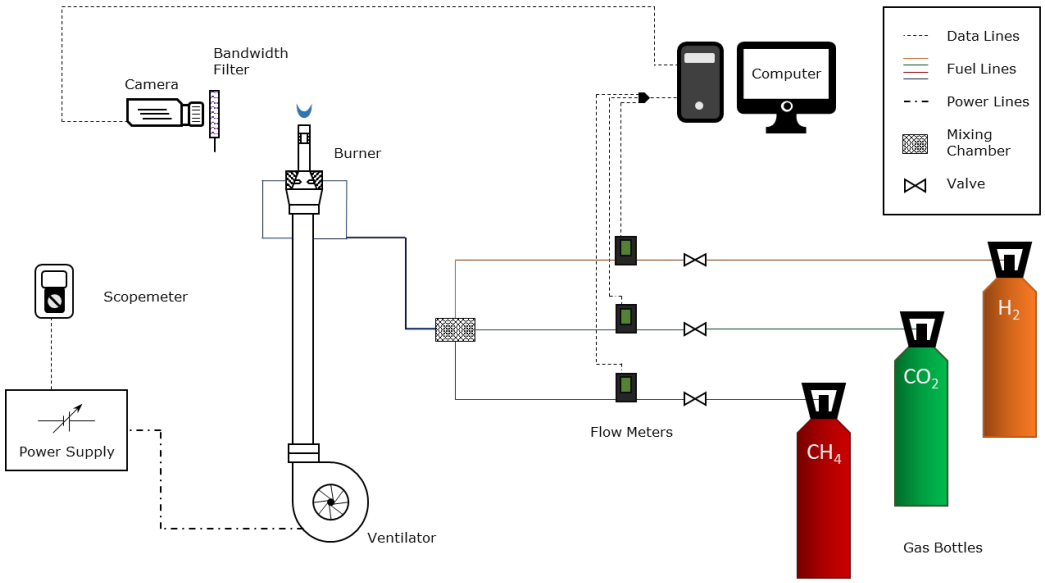

Figure 3.2: Camera and fuel system setup schematic.

3.1.2 Camera Setup

Figure 3.2 shows a schematic of the layout for the camera setup assembled, as well as the burner setup and fuel sourcing system. A JAI CV-M9GE RGB camera, capable of a resolution of 1024x768 pixels, was used for the flame photos attached to a Nikon AF Nikkor 50mm f/1.4D lens. JAI's own JAI Control Tool was used as the image capture software. The lens aperture was set to the highest setting possible, f/1.4, and both zoom and focus calibrations were made with the use of a graph paper target.

The bandwidth filters were placed on a holder in front of the camera lens, with the aim of defining the location of the forming substances, and from there deducing flame shape. 3 types of filters were used, each restricting the incoming light to a substance's formation specific wavelength. The filters used had a bandpass centre wavelength of 516nm (Andover 515FS10-50) for the C_2 images, 431nm for the CH images (Andover 430FS10-50) and 451nm for the CO_2 images (Andover 450FS10-50). The fuels used for the pictured flames and their respective compositions will be further discussed in section 3.4.

3.1.3 PIV Setup

Particle Image Velocimetry (PIV) studies were undertaken as a non-intrusive way of defining the LSB flowfield for this particular installation. PIV allows for the measurement of the flow characteristics by illuminating the pre-seeded interest region through a pair of laser beams within a defined interval of each other. This illuminates the seeded flow, and defines two flow conditions from which flow data can be assessed. A synchronized camera then captures the two flames, and from a sample of pairs, by defining the scale factor, the local velocity can be defined for the laser plane.

The overall layout of the PIV setup is similar to the camera layout albeit with some fundamental differences. While the camera layout was conceived for studies of a reacting flow, the PIV tests were undertaken using a non-reacting flow. This overrides the necessity for fuel supply, but adds the necessity

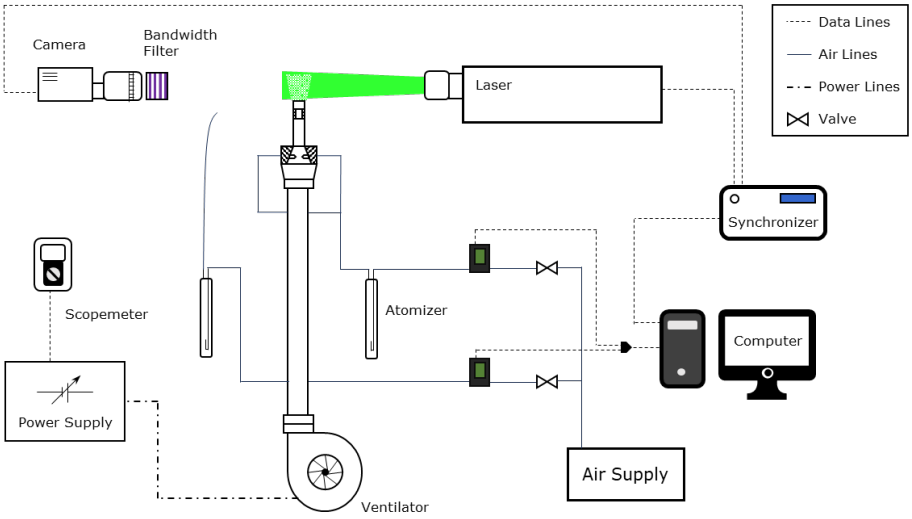

Figure 3.3: Non-reacting PIV setup schematic.

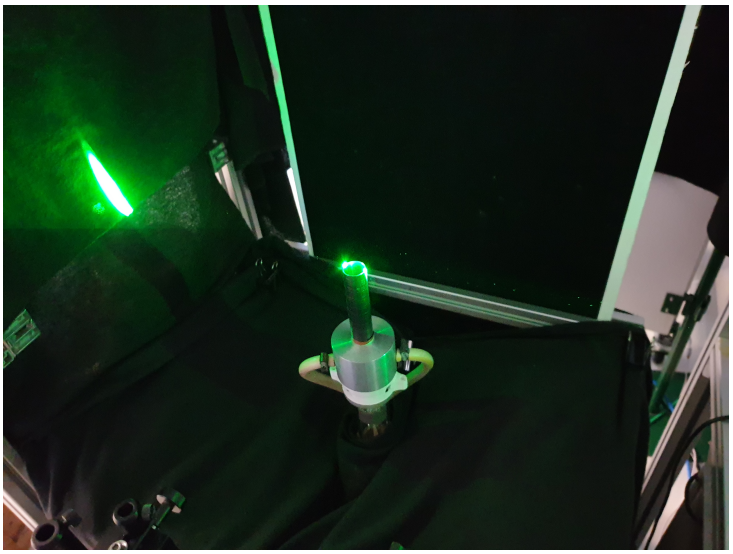

Figure 3.4: Burner under PIV analysis (Laser visible).

for an air supply to provide the seeding particles for the PIV tests.

For this application, liquid paraffin was used to provide the seeding. The paraffin was atomized into particles through a pair of atomizers, reusing the aforementioned Alicat flow meters for the necessary air supply (dry air was supplied to the flow meters through a compressor). One of the atomizers was then connected to where the fuel inlet would be, while the other slowly released particles to fill the environment surrounding the burner outlet. This was made with the aim of reducing uncertainty in the outer shear layer between the seeded burner flow and the external environment. The external environment was enclosed with light absorbent blankets, both to keep the stagnant environment undisturbed, and to prevent any external light from causing reflections which may disrupt the results. Figure 3.3 shows a simplified schematic of the PIV setup layout.

The laser used to illuminate the particles was of the Dantec DualPower 65-15 Nd:YAG type, synchronized to an ANDOR Zyla 5.5 sCMOS camera through a BNC Model 575 synchronizer. The laser has a

Figure 3.5: Pair of swirlers of the same geometry. The swirler on the left was produced by injection moulding, the one on the right by 3D printing.

beam wavelength of 532 nm, and is capable of a maximum frequency of 15 Hz. The camera made use of a Nikon AF Nikkor 60mm f/1.28D lens, set to its largest aperture (f/1.28), coupled to a Meller Griot bandwidth filter of 532nm wavelength to protect the lens from overexposure and filter undesired noise, and is capable of obtaining images with a resolution of 2560x2160. The laser intensity was established by trial and error, and was adjusted until the seeding was adequately visible. The focus of the camera was then adjusted using a graph paper target positioned where the laser beam would be in operation. All results were obtained and processed using the Dantec DynamicStudio 5.1 software.

For the tests of the plane tangent to the burner exit, as the flow was non-reactive and the particles were considered to not suffer from significant diffusion effects, the whole burner setup was rotated 90^o to obtain the flow velocities. The laser beam was aligned with the burner outlet without illuminating it, illuminating the particles directly downstream of the outlet instead. The axis of the camera was then lined up with the axis of the burner exit, and a protective screen was introduced, together, again, with light absorbent cloaking to prevent any reflections.

3.2 Swirler Selection

As described previously, the swirler is a small piece consisting of two separate regions: a central axial flow region, restricted by a perforated centre screen designed to induce a pressure loss in the inner annulus of the flow, and a number of vanes on the outer annulus designed to induce a tangential velocity to the outer annular flow.

The laboratory had available a pair of polymer swirlers from a previous installation using the same burner end, the dimensions of which are shown in Figure 3.6, produced by injection molding. These swirlers fit in the 25.4 mm (1 in) burner outlet diameter, and have 8 vanes at a fixed angle of 37^o. Therkelsen et al. obtained ideal results for vane angles of $30^o < \alpha < 42^o$ for hydrocarbons, and $30^o < \alpha < 35^o$ for high-hydrogen fuels to decrease the risk of flashback, and hence the swirler keeps a good compromise for the test fuels [13]. The centre section is 20 mm in diameter, and the screen that covers it is perforated with circular holes 1.5 mm in diameter, laid out in a square pattern, spaced at regular

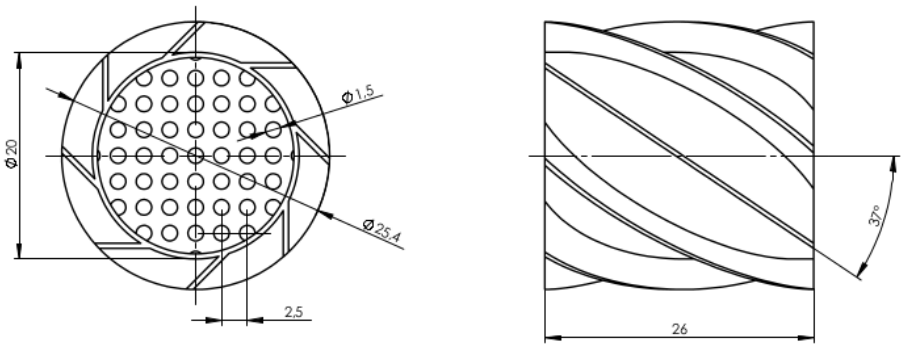

Figure 3.6: Technical drawing of 1 in diameter swirler and primary dimensions (in mm).

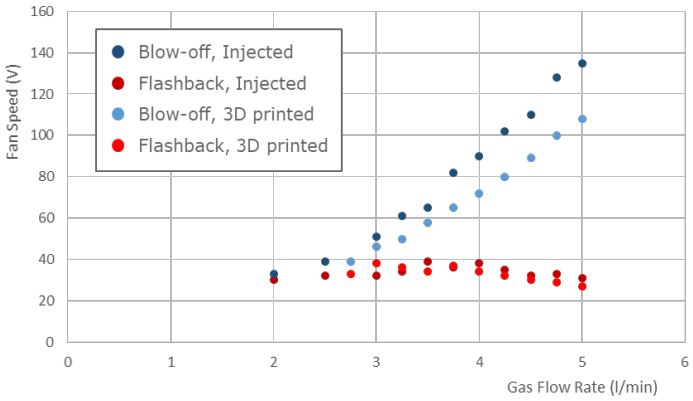

Figure 3.7: Swirler stability limits comparison for an Injection moulded and a 3D printed swirler.

2.5 mm intervals in both the x and y directions. This results in a screen blockage of roughly 74% of the total area.

Another swirler was 3D printed as a test comparison using ASA-X polymer to the exact same geometry specifications. The goal of this was to study the feasibility of 3D printing for swirlers, as it allows for a much greater level of customization and geometry variation. For example, a change in the centre screen pattern, namely with the use of fractals, has been shown to improve the stability limits when compared to circular pattern perforated screens, especially for flames with the addition of hydrogen [30].

The stability limits of both swirlers were then measured for a pure propane flame to assess the similarity between the two production methods. Tests showed (Fig 3.7) the 3D printed swirler to have similar, if not slightly narrower flashback limits, and visibly higher blow off limits, resulting in markedly tighter stability limits overall. This is mainly due to its noticeably worse surface roughness, and its larger vane thickness, increasing the turbulence levels, and leading to quenching of the flame at higher levels of ϕ. As a consequence of this, the injection molded swirler was chosen for the tests, and the possibility of 3D printed swirlers was discarded.

Swirler Position

The position of the swirler inside the burner is measured by a parameter L_i, named swirler recess, which measures the axial distance between the top of the swirler and the burner outlet.

Despite showing a relatively small effect on the flow characteristics when compared to other geometric parameters of the swirler, previous studies recommended maintaining an interval of $2R_b < L_i < 3R_b$ as acceptable values of swirler recess [13]. More recently, however, it has been shown that an increase in swirler recess inside the burner can have an effect similar to that of decreasing the swirl number [31]. Tests showed, as will be presented in Section 4.1.2, a swirl number for this particular setup of roughly 0.5, which puts it within the low swirl regime. Furthermore, it was considered that, due to the relatively small axial velocities of the tested flows, a larger recess could lead to a mixing of the centre and annular flows, deforming the desired flow field. Therefore, a swirler recess of $2L_i$ was enforced.

3.3 Processing

3.3.1 Image Processing

The flame images were obtained as .tiff files, with a gain of 150 for images without filter and 425 for images with filter. A set of 36 conditions was then defined for testing, by adding a molar fraction of 0, 10, 20 and 30% H_2 to pure methane and two compositions of biogas (80/20 and 60/40), each for a ϕ of 0.9, 1 and 1.2. A more detailed insight of the fuel composition and properties is present in Section 3.4. The mixture of pure CH_4 with 30% H_2 was deemed at risk of flashback for the $\phi = 1.2$ condition, and images could not be obtained safely for that condition. For each condition, a set of 5 images was obtained so as to allow the calculation of a more representative average of the flame at each set point.

The obtained images were then processed using the ImageJ software. In a first instance, the 5 images for each case were averaged, and each type was then processed separately. All cases had visibility issues for leaner flames, which would cause the software to struggle with defining flame boundaries. Therefore, each type of photo was processed using its specific process, in order to make sure the flame was visible under all conditions, while still keeping the pictures of the richer flames from saturating.

Therefore, for the flame photos with no filter (named "Blank"), a brightness scaling of 0-200 was performed (from the original 0-255 range), at which point the image was converted into an 8-bit scale (by averaging the red, green and blue channels). This darkened the image, as there is virtually no red light emitted from the flame. Thus, a new brightness adjustment for 0-132 was performed, and a threshold of 18-255 was set. This allowed the "Analyze Particles" function of Image J to locate the contours of the flames.

As the C_2 filter allowed very little light to come through, a very small brightness scale of 1-33 was used. Despite this, flames at ϕ=0.9 were barely discernible, and neither a higher intensity threshold nor a lower threshold could properly localise the flame. While the high threshold would not acknowledge the flame, the low threshold would also pick up background noise, precluding the identification of the flame outlines in this case. For the flames at other equivalence ratios, the colour channels were separated, as

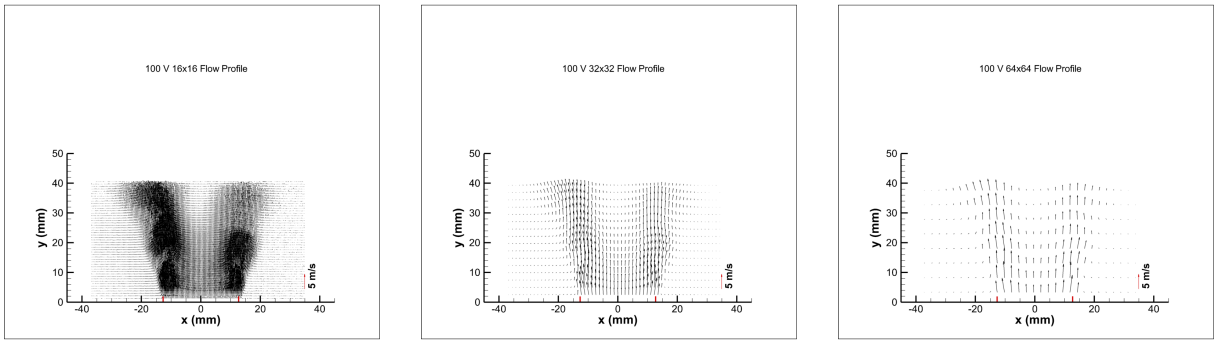

Figure 3.8: Flow field results for 100 V, and interrogation areas of size 16x16, 32x32 and 64x64, respectively.

the flame is purely green in colour, and the green channel was converted into an 8-bit black and white image. For this image, a range of 36-255 was then defined to establish the flame outlines.

Similarly, for both CH and CO_2 bandwidth filter pictures, a brightness modification was applied (7-94 for CH; 8-84 for CO_2), and only the blue channel was considered, as the flames were shown to be mainly blue. From there, a threshold of 20-255 was defined for flames taken with the CH filter, and 18-255 for the CO_2 ones, and again, the "Analyze Particles" function was used to define the flame outlines.

3.3.2 PIV Data Processing

The PIV images were acquired in sets of 400 pairs of images at a frequency of 15 Hz, with a time between pulses of 20 ms. This generated a good sample size for averaging flow speeds at a reasonable time expense. The images were then masked to include only the interest area, and dimension calibration was made using a graph paper target. With this scale factor defined, the velocity vectors could be obtained.

The velocity calculations were made using cross correlation, by dividing the image into small zones. These zones, called Interrogation Areas (IA), can be of 16px, 32px, 64px or 128px in size for both of the 2D cartesian coordinates, and the software will register the movement of each particle within this IA over the time between the two image captures. For the analysis of each IA an overlap factor of neighbouring interrogation areas can be defined, which defines an outer boundary within which the particles will be considered (and can be 25%, 50% or 75% of the IA size, for both x and y).

If the time between pulses is too large, the particles within that boundary will move over to another IA, and the results will not be valid. In addition to that, the swirling flow is a 3D flow, which means the particles of the flow are moving not only along the laser beam plane, but through it. Bearing these two restrictions in mind, the time between pulses was set to be relatively low, reducing the risk of the particles moving on into other areas and being substituted by other particles entering the IA.

For this application, tests were made for 16x16, 32x32 and 64x64px interrogation areas, as shown on Figure 3.8. The smallest areas did not yield cohesive results, possibly due to the particles exiting the IA in the second frame, while the 64x64px interrogation areas did not provide the desired resolution. Thus, an IA size of 32x32 was chosen, with an overlap parameter of 25% in both the x and y directions.

Cross correlation was then performed for each of the image pairs, and outliers were discarded by way of a maximum value filter. The 400 individual results were then averaged to provide the flow field for each case.

3.4 Fuel Test Conditions

For the reacting flows, and bearing the purpose of studying flame stability in mind and ensuring the results are comparable, fuel conditions were set so that two main criteria were met:

1. The molar fractions of the components of the fuel were set beforehand and kept constant, so that a good comparison on the impact of the variation of each component could be obtained;

2. The power of the flame was kept constant between all tests.

A set of 12 conditions were then set. To simulate biogas, two mixtures of CH_4 and CO_2 were considered, one with 80% methane and 20% carbon dioxide, and another with 60% methane and 40% CO_2, in addition to a pure methane condition. Subsequently, 4 percentages of H_2 were mixed into the overall flow (0, 10, 20 and 30%). For a mixture of biogas constituted of A% CH_4, and consequently $(100 - A)$% CO_2, and a hydrogen percentage of B%, the molar fraction for each of the substances can be calculated as follows:

$$y_{H_2} = \frac{B}{100} \tag{3.1a}$$

$$y_{CH_4} = \frac{A}{100}\left(1 - \frac{B}{100}\right) \tag{3.1b}$$

$$y_{CO_2} = \left(1 - \frac{A}{100}\right)\left(1 - \frac{B}{100}\right) \tag{3.1c}$$

As the temperature and pressure conditions were considered to be uniform for all the species, the volume flows for each set condition, as set by the flow meters, must therefore follow these restrictions.

Since tests were made experimentally by defining the desired volume flows, the equations for molar fractions were used. Thus, the stoichiometry ratio for any biogas and hydrogen combination was given by:

$$\phi = \frac{(2y_{CH_4} + 0.5y_{H_2}) * 4.76}{\left(\frac{\dot{V}_{air}}{\dot{V}_f}\right)} \tag{3.2}$$

where $\dot{V}_f = \dot{V}_{CH_4} + \dot{V}_{H_2} + \dot{V}_{CO_2}$

Power of the flame was calculated through the lower heating value of the fuel, using Equation 2.9. A base power value was then set, to be used by all flames, calculated as the equivalent power of a pure methane flame with a fuel flow rate of 9.85 SLPM. The power for all flames was then defined to be approximately $P = 5.88$ kW. For combinations, the power equation was defined as:

$$P\frac{R_0 T}{p} = \dot{V}_{H_2} LHV_{H_2} + \dot{V}_{CH_4} LHV_{CH_4} \tag{3.3}$$

This equation was then combined with Equations 3.1 and numerically solved to calculate the necessary flow rate for each case. The flow rates for each fuel are shown in table 3.1:

Table 3.1: Fuel rates in SLPM for CH_4 (top), CO_2 (middle) and H_2 (bottom) for the flame test conditions.

Base Blend	H_2 0%	H_2 10%	H_2 20%	H_2 30%
Methane (CH_4 100%)	9.85	9.53	9.15	8.72
	0	0	0	0
	0	1.06	2.29	3.74
Biogas 80/20	9.85	9.53	9.15	8.72
	2.46	2.36	2.25	2.12
	0	1.31	2.81	4.54
Biogas 60/40	9.85	9.53	9.15	8.72
	6.57	6.22	5.83	5.4
	0	1.06	2.29	3.74

3.5 Air Flow Rate Calculation

To obtain the air flow through the burner outlet, a numerical integration process was defined to integrate the velocity profile along the outlet surface. This outlet surface is a 2D surface in polar coordinates, which means the numerical integration had to be adjusted from cartesian coordinates. The integral which yields the flow rate, considering an axisymmetric velocity profile, is defined as:

$$\dot{V}_{air} = \int_0^{2\pi} \int_0^{R_b} V r dr d\theta \tag{3.4}$$

Since the function for the velocity at the burner outlet is discrete, a trapezoidal numerical integration was used to calculate the flow rate. The trapezoidal integration formula for a function $f(x)$ for an interval $[a; b]$ divided into n sections so that $a = x_0$ and $b = x_n$, considering $\Delta x_k = x_k - x_{k-1}$ is as follows:

$$\int_a^b f(x)dx = \sum_{k=1}^{n} \frac{f(x_{k-1}) + f(x_k)}{2} \Delta x_k \tag{3.5}$$

In the radial integration a factor of r has to be multiplied by the velocity function, meaning, for the numerical integration a secondary function $g(r) = V(r) * r$ was defined and numerically integrated between 0 and R_b. To take into account the asymmetry of the velocity profile, a second integration was made between $-R_b$ and 0, which was then averaged with the positive integration and multiplied by 2π to obtain the results.

3.6 Cantera Modelling

To estimate the emissions for an LSB flame, adiabatic 1D flames were made using Cantera [32] to simulate the propagating LSB flame. Cantera is an open-source Python module for chemical kinetics and thermodynamics of combustion, and the simulations were conducted using the GRI Mech 3.0 [33] mechanism. This mechanism calculates a one-dimensional adiabatic freely-propagating flame at a pressure of 1 atm and burner temperature of 300 K by defining the reaction rates for 53 species, totalling 325 reactions. GRI Mech 3.0 is a widely used mechanism, both in an academic setting [34] and in the industry, and although more detailed mechanisms are available, it provides a good balance between result accuracy and computational cost, yielding good results for the desired species (NO and NO_2 in this case) under the test conditions [35, 36].

The simulation takes the initial conditions as input, and is considered to provide the final combustion products fraction when the adiabatic temperature is reached. The simulation was made for equivalence ratios of $0.8 < \phi < 1.2$, delivering results for the set conditions of methane, carbon dioxide and hydrogen mixtures for such variables as flame speed, adiabatic temperature and molar fraction of the combustion products. For this study, and for the LSB architecture in general, the main goal is to reduce the levels of NO_x, which were considered to be the sum of NO and NO_2, and thus the results for these levels were considered, as well as adiabatic temperature, which is related to the formation of these species, as will be further discussed in Section 4.4.

3.7 Uncertainty Analysis

The Alicat flow meters, mentioned in Sub-section 3.1.1, show an error dependant on both the set point flow and the flow meter capacity. These uncertainties are defined as:

$$U_{\dot{V}} = \pm 0.008\dot{V}_{sp} \pm 0.002\dot{V}_{max} \tag{3.6}$$

where $U_{\dot{V}}$ is the uncertainty associated with the flow rate, $\dot{V}_{sp}$ is the flow rate for a determined set point, and $\dot{V}_{max}$ is the maximum capacity flow rate of the flow meter. Since the latter is a constant for each flow meter, independent of the flow rate, the highest uncertainties, defined as the error $e_{\dot{V}}$ (in percentage) will be associated with the lowest values set for the highest capacity controllers, and the lowest error values will be associated with the highest values (relative to the capacity) of the lowest capacity flow meters. Table 3.2 shows the maximum and minimum value of error for the conditions described in Table 3.1, keeping in mind the flow meter capacities for each fuel (described in Section 3.1.1).

The hydrogen flow rate was controlled using 2 flow controllers mounted in parallel, as the 5 SLPM capacity was lower than the maximum flow necessary. The uncertainty when using both controllers was then calculated by adding the uncertainty of the two controllers at the set points (one opened fully, the other at a partial load of 0.79 SLPM). If only one controller was used, the uncertainty is calculated as normal, seeing that the closed controller has no influence in the flow rate. This case was found to contain both the lowest and the highest uncertainty, since, for the single case where both flow meters were used,

Table 3.2: Maximum and minimum uncertainties for each fuel species.

	Gas	$\dot{V}_{sp}$ $(SLPM)$	$\dot{V}_{max}$ $(SLPM)$	$U_{\dot{V}}$ $(SLPM)$	$e_{\dot{V}}$
Maximum	CH_4	8.1	20	$\pm$0.1048	1.294%
	H_2	1.06	5	$\pm$0.0185	1.743%
	CO_2	2.12	50	$\pm$0.1170	5.517%
Minimum	CH_4	9.85	20	$\pm$0.1188	1.206%
	H_2	4.54	5	$\pm$0.046	1.020%
	CO_2	6.57	50	$\pm$0.1526	2.322%

the error associated with the flow meter capacity was doubled, increasing the uncertainty, yet the total flow rate was the largest of all cases studied, reducing the error. This meant the error ($\pm$ 1.145%) was within the range of errors of the single flow meter cases.

These uncertainties affect the fuel mixture parameters, namely ϕ and the molar fractions of H_2 and CO_2. To calculate the uncertainties on these, the error propagation formula is used. The uncertainty for CO_2 is given by:

$$U_{y_{CO_2}} = \pm \frac{\dot{V}_{CO_2}}{\dot{V}_{CH_4} + \dot{V}_{CO_2}} \sqrt{\left(\frac{U_{\dot{V}_{CO_2}}}{\dot{V}_{CO_2}}\right)^2 + \left(\frac{\sqrt{U^2_{\dot{V}_{CO_2}} + U^2_{\dot{V}_{CH_4}}}}{\dot{V}_{CH_4} + \dot{V}_{CO_2}}\right)^2} \tag{3.7}$$

Using this formula, the maximum uncertainty for the CO_2 fraction can be calculated as:

Table 3.3: Maximum y_{CO_2} uncertainty, error and conditions.

$\dot{V}_{CH_4}$ $(SLPM)$	$\dot{V}_{CO_2}$ $(SLPM)$	$U_{y_{CO_2}}$	$e_{y_{CO_2}}$
8.48	2.12	$\pm$0.01143	0.539%

The uncertainty for the hydrogen molar fraction can be calculated in a similar way, taking into account the flow rates and uncertainties of both CH_4 and CO_2:

$$U_{y_{H_2}} = \pm \frac{\dot{V}_{H_2}}{\dot{V}_{CH_4} + \dot{V}_{CO_2} + \dot{V}_{H_2}} \sqrt{\left(\frac{U_{\dot{V}_{H_2}}}{\dot{V}_{H_2}}\right)^2 + \left(\frac{\sqrt{U^2_{\dot{V}_{CO_2}} + U^2_{\dot{V}_{CH_4}} + U^2_{\dot{V}_{H_2}}}}{\dot{V}_{CH_4} + \dot{V}_{CO_2} + \dot{V}_{H_2}}\right)^2} \tag{3.8}$$

And the maximum uncertainty for hydrogen molar fraction was calculated as being:

Table 3.4: Maximum y_{H_2} uncertainty, error and conditions.

$\dot{V}_{CH_4}$ $(SLPM)$	$\dot{V}_{CO_2}$ $(SLPM)$	$\dot{V}_{H_2}$ $(SLPM)$	$U_{y_{H_2}}$	$e_{y_{H_2}}$
9.53	0	1.06	$\pm$0.00243	0.229%

The air flow supply was not provided through flow meters, instead relying on the ventilator. As will be shown in section 4.1.1, the air flow rate was calculated through the integration of the velocities obtained by PIV analysis at the burner outlet using numerical methods, and an approximate curve was obtained for use in the equivalence ratio calculations. As such, the uncertainty analysis for this flow was considered not to be accurately definable, further invalidating an uncertainty analysis for ϕ.

Chapter 4

Results and Discussion

This chapter presents the studies made on the fuel flexibility of the LSB design. The first studies made measured the flow field downstream of the burner exit, comparing it to a typical LSB flow field. Photo analysis of the reacting conditions is then presented, together with the analysis of the effects of the addition of hydrogen, carbon dioxide and a mixture of both to the base methane flame. Flame parameters such as position, shape and brightness are discussed.

Stability limits are then established for the same conditions as the photos, and the effects of fuel composition on the stability limits are discussed. Finally, a simulation of the emission levels is presented for each case, and results are evaluated.

4.1 Non-reacting PIV Flowfields

Non-reacting PIV studies were made to define the flow field at the burner's outlet, specifically, in both a plane perpendicular to the outlet, aligned with a centreline of the burner, and a plane parallel to the burner outlet at the minimum distance achievable. This distance was estimated to be less than 2 mm, and the plane was effectively defined as the $x = 0$ plane. For coherence in the results, this distance was also discounted in the perpendicular plane, and the origin was defined as being the intersection point between the centreline of the burner and the $x = 0$ plane. For the study of the flow for an (x, r) plane, an area of interest was defined for a radius of 25 mm from the axial centreline and a distance of 40 mm from the burner outlet, while for the (r, θ) plane, the area of study was defined as a circle centred at the origin with a radius of $r = 12.7$ mm.

To calculate the flow rates, flow fields are considered to be axisymmetric around the normal axis to the burner outlet. Although results for the plane tangent to the burner outlet show a clear imprint of the guide vanes on the tangential flow vector map, the effect of these on the global flow rate was not considered, as the imprints are relatively small when compared with the overall domain. As mentioned, a pre-seeded environment was created by introducing paraffin particles similar to those introduced into the burner in the environment around it, and allowing the particles to settle before running the tests.

As an example, in Figure 4.1 it is perceivable that the flow field for unseeded results shows a very

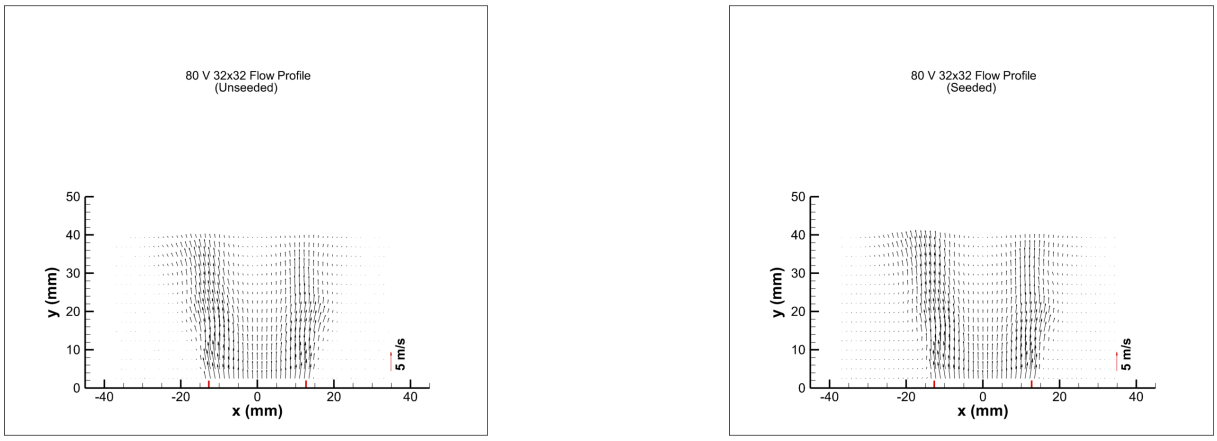

(a) Unseeded environment

(b) Seeded environment

Figure 4.1: Comparison of seeded vs. unseeded environment (80 V)

abrupt velocity difference between the swirling flow and the environment, which would indicate a very strong turbulent shear layer in this region. However, further testing with the pre-seeded environment was made, which showed a much smoother transition, and much more in line with the expected results for an unconfined flow at the tested Re [16]. Further tests were then made for 10 different ventilator voltage levels: 30, 40, 60, 80, 100, 110, 120, 130 and 140 V, as Figures 4.2 and 4.3 show.

Flow field analyses show a well defined Low Swirl environment both in the horizontal and vertical planes, and in both cases the lower velocity axial flow centre section and the higher velocity annular swirled flow section are distinguishable in all cases, providing cup-shaped streaklines on the (r, x) plane, on which, considering constant S_T, a flame can stabilize, forming the typical cup-shaped LSB flames.

The velocity gradient between the two sections is smaller than that between the swirled flow and the stagnant environment, primarily due to the swirler recess inside the burner, but also due to the relatively small scale of the burner, which allows the flow to reduce this abrupt velocity difference. This effect is noticeable in both flow field map types, but can be better perceived in the vertical plane map.

The results in the (r, x) plane also showed the divergence of the flow, exhibiting a noticeable radial component to the velocity, particularly in the outermost part of the swirled annulus. This causes the flow to expand in the radial direction into the environment and slightly increase the size of inner annulus x, sharply reducing axial velocity of the overall flow. This is one of the staples of the low swirl burner's adaptability, as the divergence of the flow allows the flame to stabilize at the location where the flow velocity is equal to the turbulent burning velocity S_T, regardless of the conditions which affect it (such as ϕ or the fuel properties). Results also show, particularly for the higher velocities (120 V, 130 V and 140 V), a very low velocity area in the centre of the flow, showing that this particular flow field is at a swirl number on the upper scale of low swirl, almost generating a recirculation bubble. Although the non-reacting PIV results don't show it, other studies have shown that the reacting flow causes the acceleration of the flow due to gas expansion at the flame brush, which, due to the larger velocity of the outer annulus, may cause stagnation of the flow or even a small recirculation zone as the divergence effect decreases [14, 16]. Nevertheless, this recirculation zone is not particularly important for the flow as it

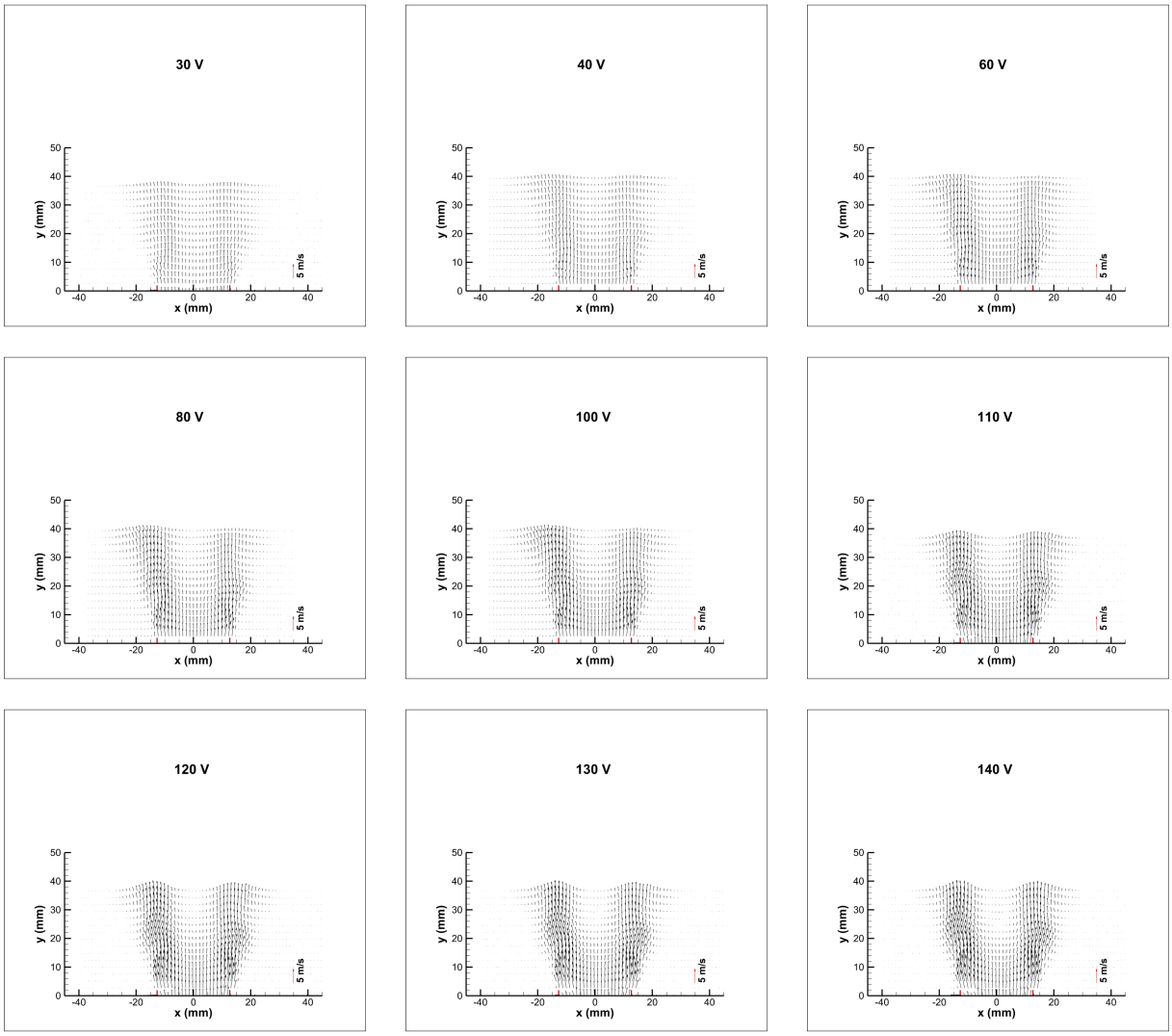

Figure 4.2: Vector plots for the (x, r) plane. Left to right; top to bottom: 30 V, 40 V, 60 V, 80 V, 100 V, 110 V, 120 V, 130 V, 140 V.

generates downstream of the flame brush, meaning the main stabilization mechanism is flow divergence.

The velocity profiles at the burner exit also show similar results. A clear distinction between the non-swirled centre and the tangentially swirled annulus can be recognized, more clearly in the tangential flow profile than in the axial one.

Moreover, both the flow field map results and the profile results show that the flow characteristics remain largely the same for all ventilator voltages, with the velocity vectors changing largely only in scale, except for the 20V case, as this low voltage yields a relatively small fan speed, leading to very small bulk velocity and a flow resembling a plug type flow rather than a typical swirling flow. This particular result was therefore discarded from any calculations relating to the swirling flow, especially seeing as flow velocities this low weren't used in any of the flame tests. However, the flow rate was taken into account, particularly in Section 4.1.1, as the axial flow rate is independent from the flow geometry.

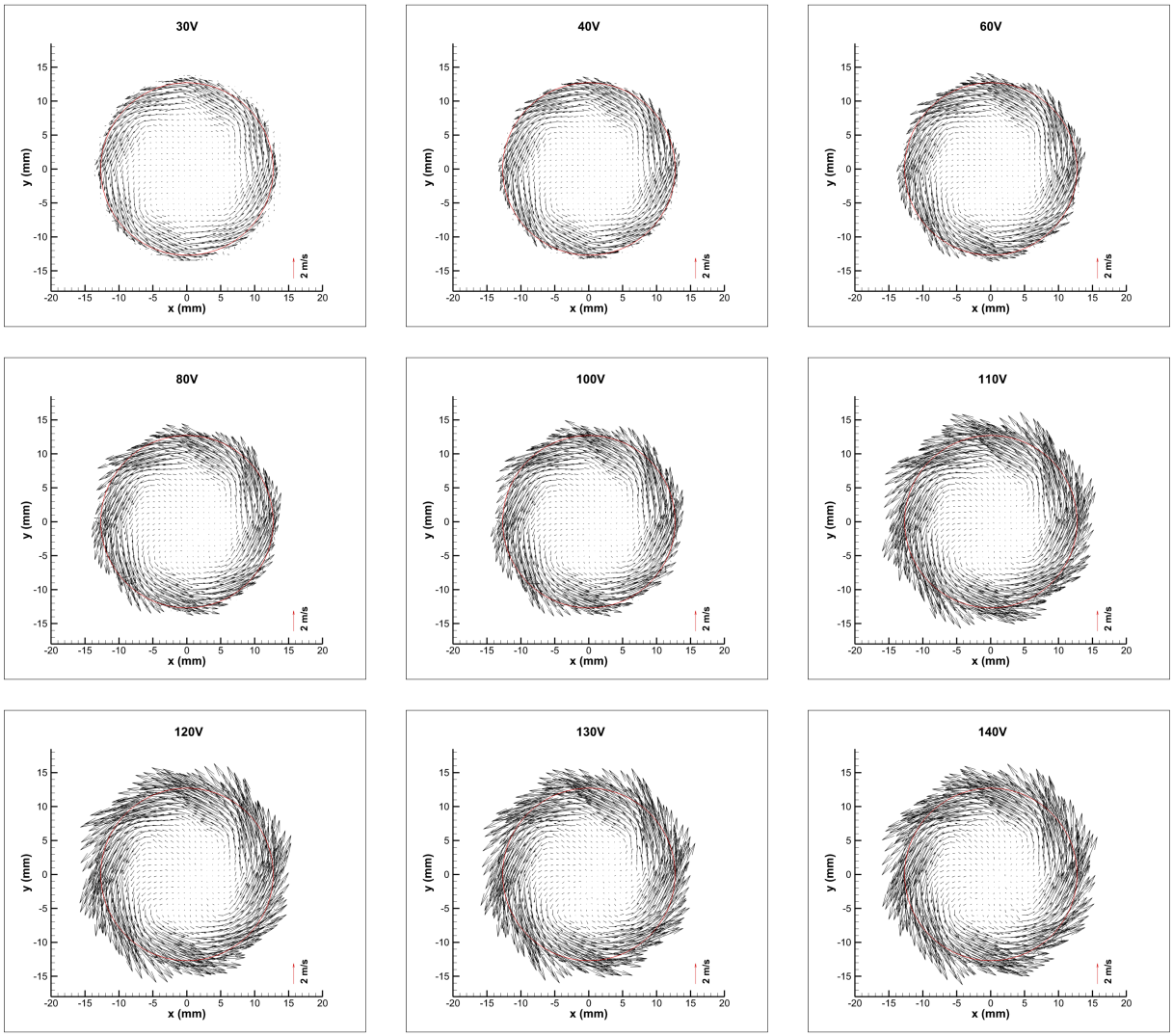

Figure 4.3: Vector plots for the (r, θ) plane. Left to right; top to bottom: 30 V, 40 V, 60 V, 80 V, 100 V, 110 V, 120 V, 130 V, 140 V.

4.1.1 Ventilator Calibration

With the velocity profiles defined, the calculation of the axial flow rate can be made by simply integrating, in cylindrical coordinates, the axial velocities within the burner diameter as discussed in section 3.5. As mentioned in chapter 3, the laboratory tests were considered to be at ambient conditions, and therefore these results can be considered to be standard results in line with the calculated flow rates based on the flow meter values. From this flow rate an average bulk velocity can be determined, and from Equation 2.5 the Reynolds number can be calculated.

Table 4.1: Calculated values of flow rate (LPM) and respective Re.

Voltage (V)	30	40	60	80	100	110	120	130	140
Flow Rate (LPM)	0.458	0.490	0.489	0.488	0.462	0.562	0.543	0.522	0.505
Re	3026	3953	5135	5952	6597	6903	7171	7401	7641

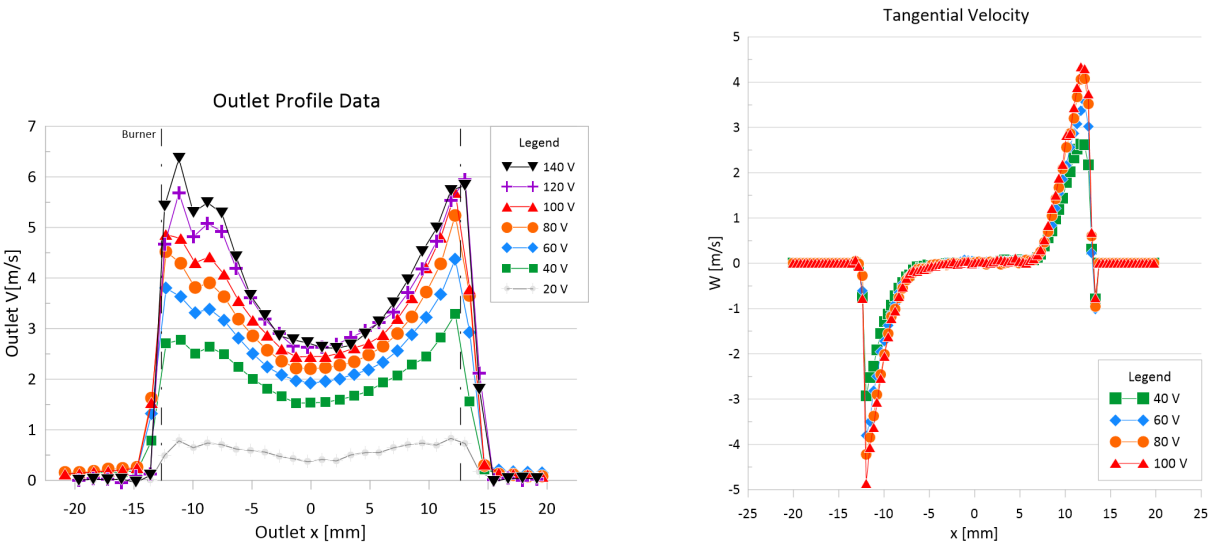

(a) Axial Profiles

(b) Radial Profiles

Figure 4.4: Axial velocity and tangential velocity profiles at the burner exit centreline.

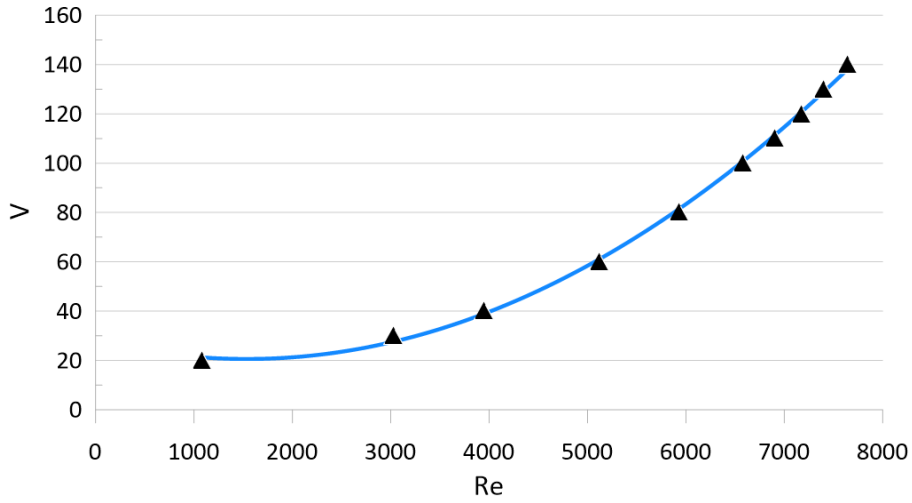

Figure 4.5: Inverse of Re in function of voltage, and respective fit curve.

Figure 4.5 shows the points corresponding to the calculated Re for each voltage setting, showing an apparent quadratic correlation between the voltage and Re (and thus the flow rate). This is coherent with the pressure loss equations in partially obstructed pipes, which assert $\Delta p \ \alpha \ V^2$ [37]. From this result, and with the aim of obtaining a better fit, the variables were switched to obtain an equation for voltage as a function of Re. The curve fit found was $V_{vent} = 3e-6 * Re^2 - 0.0097 * Re + 28.03$, with a coefficient of determination of $R^2 = 0.99885$, and that equation was numerically solved in order to obtain Re as a function of the voltage.

4.1.2 Swirl Number Verifications

Having obtained the profiles of the velocity in both the perpendicular and parallel planes to the burner exit permitted the calculation of the Swirl Number using either of the previously defined equations (Eq. 2.1 or Eq. 2.6). Since both velocities profiles are obtained at the same section, contained within the

same straight line, the results could be coupled to define the (U, V, W) components for this section. An adjustment had to be made though, as the measured points in the radial dimensions did not perfectly line up. Since the tangential velocity measurements had a better resolution as a result of having a larger number of points, the tangential velocity for the axial velocity measurement points was obtained through a linear interpolation. For any point r_j where the axial velocity V is known, and two points r_i and r_{i+1} where the tangential velocity is known, so that $i < j < i + 1$, the tangential velocity at j is given by:

$$W(j) = \left(\frac{W(r_{i+1}) - W(r_i)}{r_{i+1} - r_i} \right) (r_j - r_i) + W(r_i) \tag{4.1}$$

As more complete data was available, it was considered that there was no need for the use of the approximation of Equation 2.6. Thus, combining Equations 2.2a and 2.3 with Equation 3.5, for a set of n points, enabled the calculation of the fluxes of momentum numerically as follows:

$$G_\theta = 2\pi\rho \sum_{i=0}^{n-1} \frac{1}{2} \left[(W_{i+1} U_{i+1} r_{i+1}^2) + (W_i U_i r_i^2) \right] (r_{i+1} - r_i) \tag{4.2a}$$

$$G'_x = 2\pi\rho \sum_{i=0}^{n-1} \frac{1}{2} \left[\left(\left(U_{i+1}^2 - \frac{1}{2} W_{i+1}^2 \right) r_{i+1} \right) + \left(\left(U_i^2 - \frac{1}{2} W_i^2 \right) r_i \right) \right] (r_{i+1} - r_i) \tag{4.2b}$$

The swirl numbers were then calculated for the nine measured voltage settings. As expected, results showed the swirl number to be roughly constant around an average value of 0.5, which is a typical value for low swirl burner setups [13].

Table 4.2: Calculated values of swirl number.

Re	3026	3943	5119	5932	6577	6903	7171	7401	7641
Swirl Number	0.458	0.490	0.489	0.488	0.462	0.562	0.543	0.522	0.505

4.2 Flame Characteristics

Flame photos were obtained for the fuel conditions described in Section 3.4, for equivalence ratios of $\phi = 0.9$, $\phi = 1$ and $\phi = 1.2$. In addition to that, pictures using 3 types of bandwidth filter were taken for a total of 140 pictures. As both the power and the fuel composition were firmly defined, the air flow rate was adjusted by adjusting the ventilator voltage. However, the Reynolds numbers for all tests did not differ widely, and were well within the same order of magnitude, which, in conjunction with the results of Section 4.1 assures similarity of the flow across all conditions. As previously mentioned, flames composed of 70% CH_4 and 30% H_2 were considered to be at risk of flashback at $\phi = 1.2$, and no results were attained.

Flames at a stoichiometric equivalence ratio with no filter are represented in Figure 4.6, and they show the effects of fuel composition on the flame size, shape, position and brightness. For a particular composition of fuel, a number of parameters can influence any, or all in fact, of these characteristics.

As a method of analysis, the first impact studied will be that of the variation of hydrogen in the fuel.

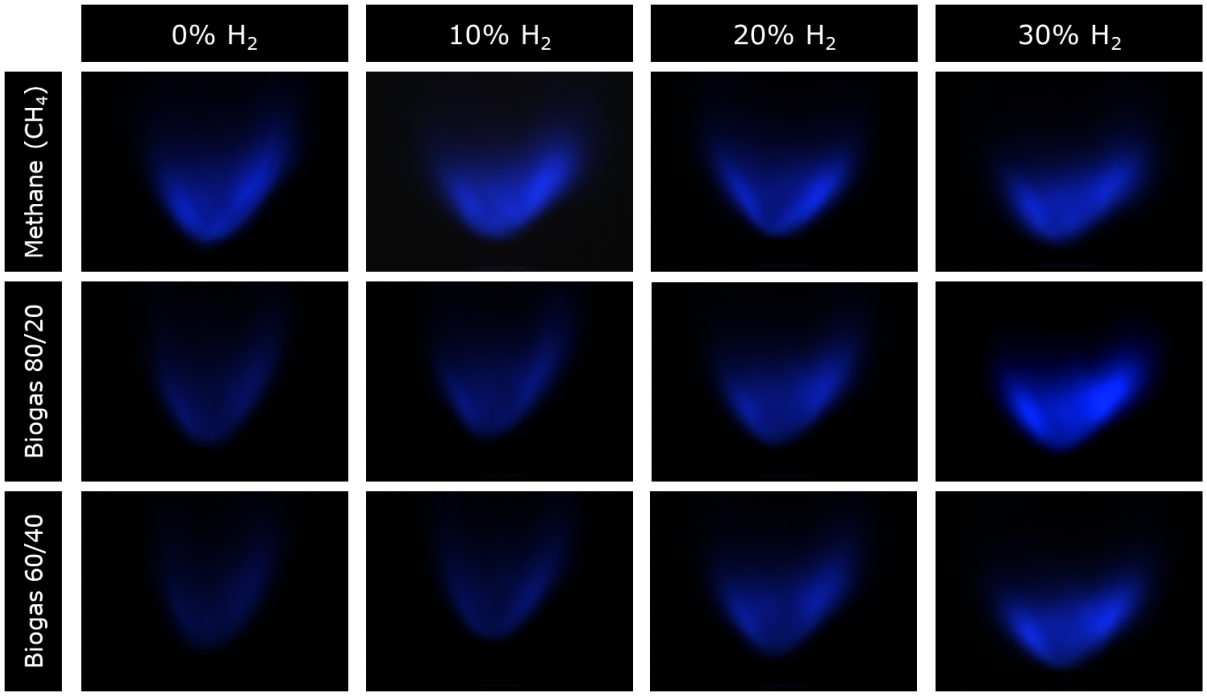

Figure 4.6: Unfiltered flames for $\phi = 1$. Top Row: Methane; Middle Row: 80/20 Biogas; Bottom Row: 60/40 Biogas. Left to Right: 0, 10, 20, 30% H_2.

As mentioned in Section 2.2, hydrogen is an extremely volatile fuel, particular for its faster combustion chemistry, and consequent high flame speed.

Flame shape, size and position can all be examined in a more intuitive manner by way of the brightness contours created for each composition of flame. As the most representative example of flame shape change for these conditions, the outlines of the four hydrogen percentages for a 60/40 mixture of biogas were chosen, and are represented in Figure 4.7. The outlines are coloured in a brighter shade of blue for an increased percentage of hydrogen, with the black outline corresponding to 0% H_2 and the lightest outline corresponding to 30%.

From the outlines, 3 conclusions are easily drawn. The first is that an increase in hydrogen fraction largely corresponds to a much more easily visible flame. This is associated with the higher brightness levels for greater hydrogen fractions, largely in part due to its fast combustion rate. The second is that an increase from 0% H_2 to 10% anchors the flame slightly downstream, a result which is counter-intuitive with the tendency for hydrogen addition. However, if the hydrogen percentage was to be further increased, the flame would move upstream and settle at a position where the flow velocity is higher, a result of the effect of its higher flame speed on the fuel.

Another significant effect noted was the widening of the flame as the H_2 percentage rose. Due to the previously mentioned characteristics of hydrogen, in particular the quick combustion mechanics, hydrogen flames tend to be shorter than those of hydrocarbons, which leads the flame to propagate in the axial direction. This results in wider, yet flatter flames and can, together with the increased flame speed, cause the flame to anchor at the burner outlet.

Figure 4.6 shows clearly that the effects of hydrogen are much more appreciable for higher levels of

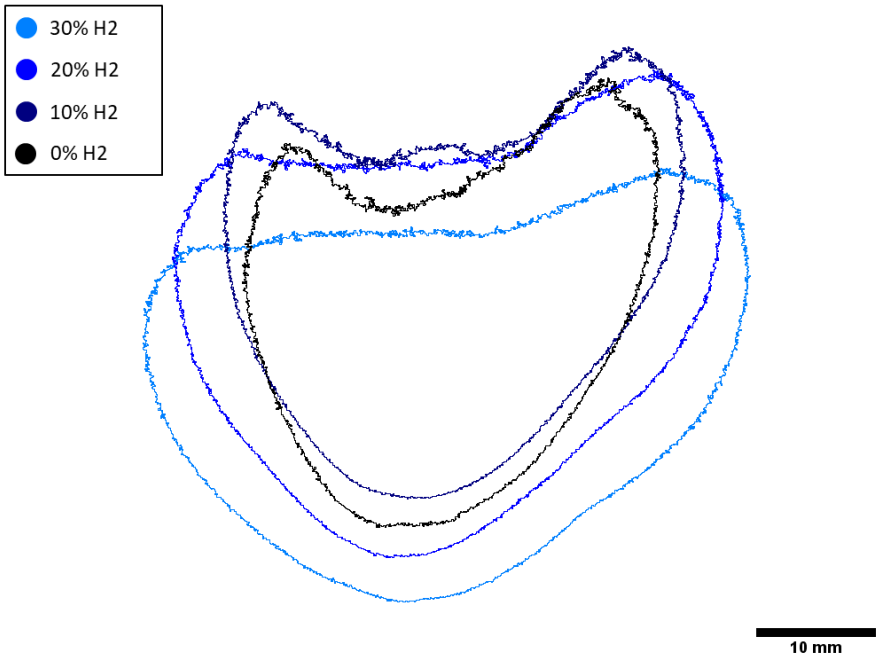

Figure 4.7: Flame outlines for a 60/40 biogas mixture and 0, 10, 20, 30% H_2 at $\phi = 1$.

CO_2 composition, as the effects of the smaller kinetic inertia of hydrogen are more noticeable when in combination with the higher inertia of the methane/carbon dioxide mixture, and hence why the contours of 60/40 biogas composition were chosen as an example.

Effects of CO_2 are also observable by comparing the flames in the columns of the grid. An increase in carbon dioxide fraction has the reverse effects of hydrogen addition: the inert nature of CO_2 draws energy from the flame, reducing its brightness [34]. Furthermore, the slower combustion chemistry of biogas leads the flame downstream and into a more closed and elongated, tulip-like shape, as opposed to the wider, shorter bowl-like shape of high CO_2 percentage flames.

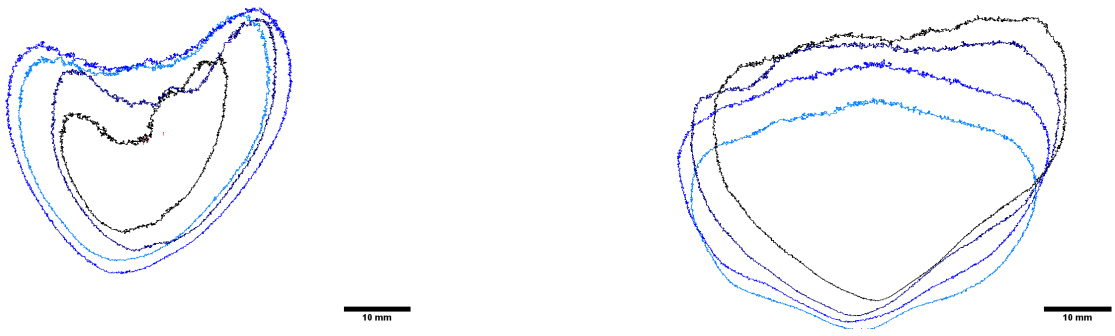

(a) $\phi = 0.9$ (b) $\phi = 1.2$

Figure 4.8: Flame outlines for an 80/20 biogas mixture and 0, 10, 20 and 30% H_2

Figure 4.8 confirms the conclusions drawn from the stoichiometric flames, as the flames exhibit the same general characteristics for the addition of each species. One noticeable exception is the case for 30% hydrogen in the $\phi = 0.9$ conditions, whose brightness contours are smaller than its 20% hydrogen

counterpart. This marks the start of a tendency for higher hydrogen fractions in leaner conditions which can be related to two phenomena. The first is due to the shift in radiation emission away from visible radiation, which could cause the brightness captured by the unfiltered images to appear lower than that of flames with a lower hydrogen component. Additionally, the higher combustion rate of the hydrogen, combined with the abundance of air in leaner conditions leads the fuel to be consumed faster, therefore generating smaller flames. Although these flames are smaller and dimmer than those of smaller hydrogen fraction, they are in fact of higher stability, as will be shown in Section 4.3.

A further comparison can be made between the outlines at $\phi = 0.9$ and $\phi = 1.2$. In the former, the outline shows a variation mainly in size, showing the effects of the accelerated combustion mechanics of H_2. However, in the latter, the main variation is in overall flame shape and position, meaning the flame is impacted by the increased flame speed, which draws it closer to the outlet, as well as shortening and slightly widening the flame, maintaining, however, the overall flame size.

Flame pictures for the other conditions, including the bandwidth filtered flames, largely show the same results as the ones on Figure 4.6, particularly the effect of fuel composition of flame shape and location, and the increase of brightness for the conditions with higher fraction of hydrogen, with the exception of 30% H_2 for biogas mixtures. The pictures are shown in Annex A.

4.3 Stability Limits

Previous studies have shown the effects of biogas composition and hydrogen in other types of flames, and the general consensus shows higher levels of CO_2 in the biogas composition tend to worsen flame stability by increasing the lean flame limit, causing the flame to quench at higher ϕ. This is due to the addition of an inert component with a relatively high heat capacity, while the addition of hydrogen tends to improve flame stability by lowering the lean flame limit, due to both the higher LHV and higher combustion rate. [7, 38]

To assess the effect of biogas composition, as well as hydrogen addition, lean stability tests were conducted for the conditions of Section 3.4. The flashback limits were not measured in this case as the LSB is designed for better performance while burning a lean premixed flame. Therefore, results for rich flames were not measured, and no flames under any conditions exhibited flashback for lean or stoichiometric burning. The fuel flows were set, and the ventilator was gradually adjusted to a higher velocity setting, until the flame was extinguished. This process was repeated at least 3 more times for each case until an agreeable value was reached.

Figure 4.9 shows the results obtained from the stability tests. For analysis purposes, it is convenient to split the results into two parts, and study the effects of biogas composition and the effects of hydrogen addition, and lastly a third analysis can conclude from the combined effects of both. As expected, and in agreement with previous findings for LSB setups [17], specifically for lower Reynolds numbers, the blow-off limits unanimously and monotonically rise with the increase in Re, showing the highest amplitude of results of ϕ in the region of 0.15 for the 60/40 biogas mix with no hydrogen. On the other hand, flames based on pure methane, with no addition of CO_2 tend to show less variation of blow-off limits, and for

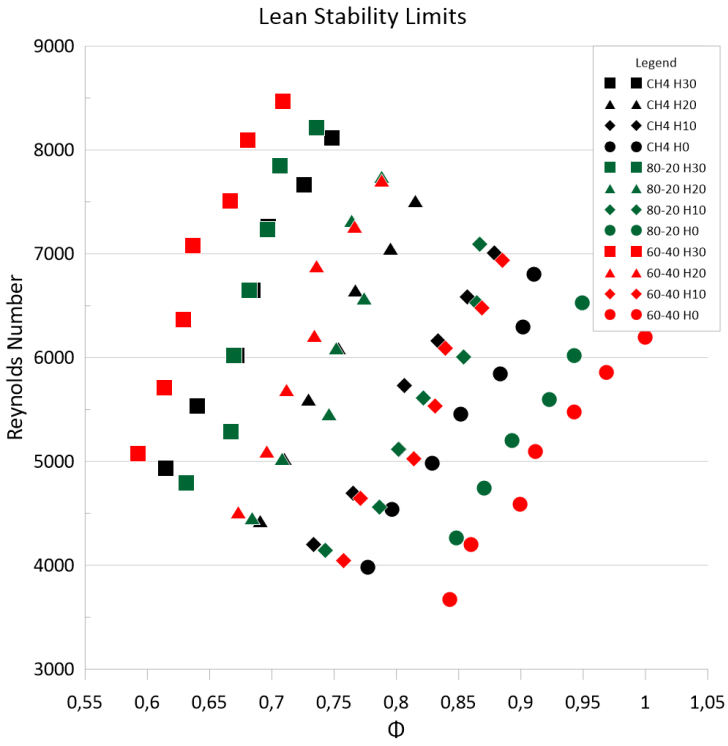

Figure 4.9: Blow-off limits for the test fuel compositions.

certain cases, such as the pure methane flames, show an inflexion towards keeping the blow off equivalent ratio constant for higher Re. As mentioned, these results are coherent with a lower Reynolds blow-off limits evolution, before hitting a maximum lean limit for Re in the order of 10000, and dropping slightly for even higher Reynolds' numbers.

The addition of hydrogen also showed the expected effect in the flame stability. Previous tests, both with LSB setups [17] and other types of burners [38] show that the addition of hydrogen significantly reduces the flame stretch rate, thereby avoiding local quenching of the flame and significantly lowering the blow-off limits of the methane/biogas flames.

A particularly interesting result is revealed when the addition of CO_2 is considered and compared to other flames with the same molar fraction of hydrogen. Flames with no hydrogen show a decrease in flame stability, significantly raising the blow-off limit, and for these conditions the addition of 40% CO_2 results in an increase of the blow-of ϕ of roughly 0.1, on average when compared to the methane flames. However, as hydrogen is added, that difference is reduced and for flames with 20% H_2 or over the biogas flames show lower blow-off limits when compared with the mixture of methane and hydrogen. Although this situation benefits from the highest value of both H_2 flow rate and total flow rate, it nonetheless shows a trend for a larger relative influence of hydrogen on biogas flames.

Another property of the LSB which was verified during testing was its sturdiness under transient conditions. As a general rule, when the fuel composition was changed, the flame simply adjusted to the position which matched the local flame speed, without the need to relight the burner. This shows the robustness and flexibility of the LSB design for a variety of fuels, and means the burner should be able to hold fluctuating fuel compositions, provided these are within the stability boundaries.

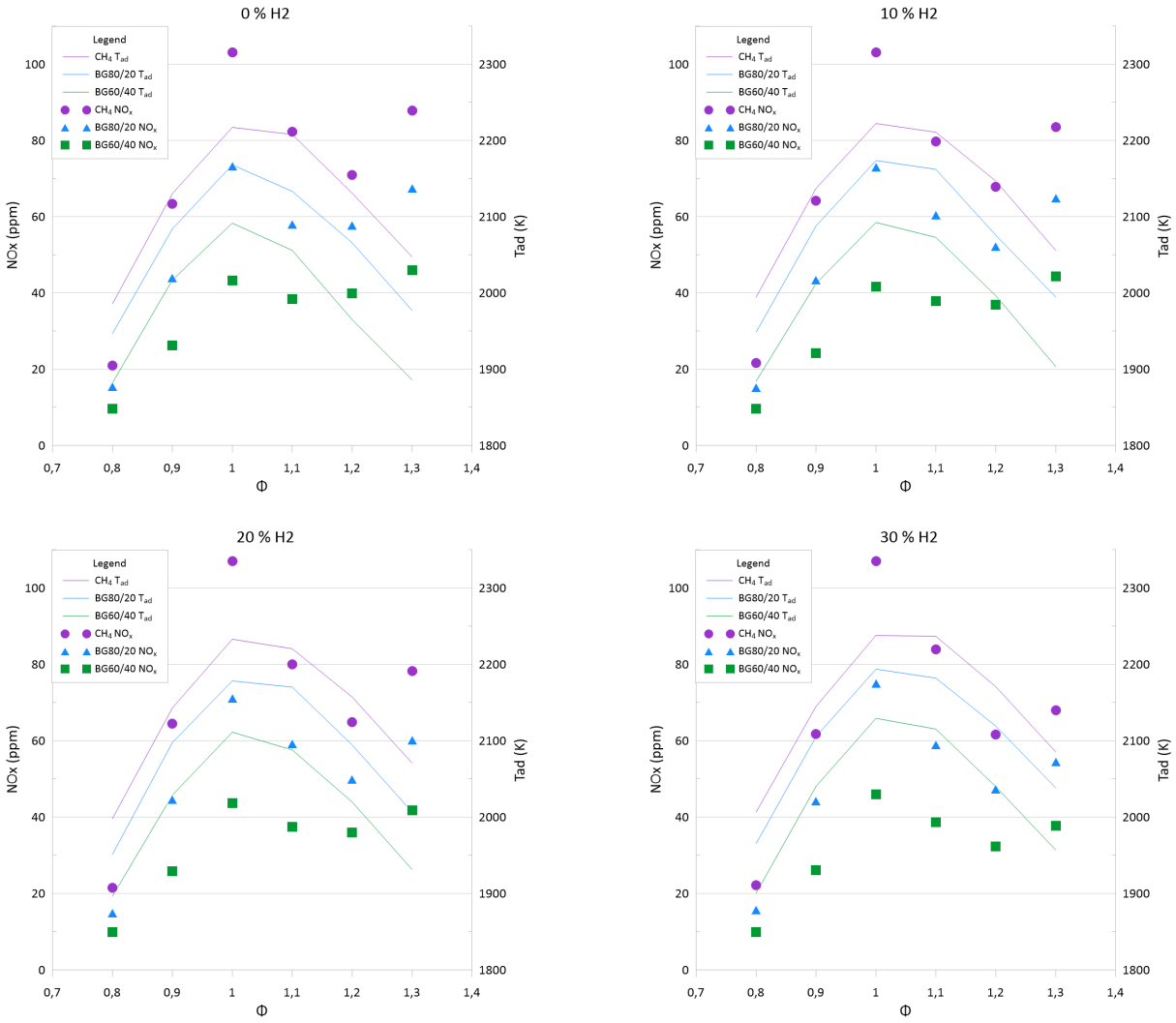

Figure 4.10: NO_x emission levels (in ppm) and adiabatic flame temperature (K) for 0, 10, 20, 30% H_2.

4.4 Emission Levels

As described in Section 3.6, simulations for a one dimensional adiabatic flame were made, meaning flow and thermal effects such as turbulence, recirculation, heat transfer and flame geometry were not considered. Although the LSB flames are not perfectly planar nor adiabatic, the propagating nature of the LSB design means its flame has been shown to be relatively well represented by the 1D approximation used in the simulations, albeit showing a better approximation for methane than for hydrogen [39, 40]. Nevertheless, the results are still relevant for the LSB combustion, as they can show trends for the changes in the parameters of interest in this study, namely, biogas composition, hydrogen addition and equivalence ratio, and provide a maximum estimate for any given condition.

Figure 4.10 shows the molar fraction of NO_x in the combustion products (in ppm) and the adiabatic temperature comparison for methane and the two biogas compositions, and their respective mixing with 10, 20 and 30% H_2. For this simulation, as a simplification, NO_x refers to the sum of the NO and NO_2 molar fractions, and constitute a harmful pollutant. NO_x is largely formed by way of one of three main mechanisms [8]: thermal (or Zeldovich), prompt (or Fenimore), and fuel. Thermal NO_x refers

to the oxides that are generated under relatively large temperatures (usually over 1600 °C), and is the mechanism by which most os the NO_x is generated under conditions close to stoichiometry. Prompt NO_x was proposed by Fenimore, and describes the mechanism by which carbon based fuels under rich conditions react with the nitrogen molecules, and this mechanism is much more significant under rich conditions. Fuel generated NO_x is relevant for fuels with a significant nitrogen fraction, which is not the case. Therefore, for this case, NO_x formation is ruled by the thermal and prompt mechanisms.

Results show a typical adiabatic temperature distribution as a function of ϕ, showing a peak around $\phi = 1$, in the region of 2200 K for methane/hydrogen fuels. Although the addition of a higher hydrogen component does not seem to affect the adiabatic temperature of the flame much, which is expected as the adiabatic temperature of H_2 is only marginally superior to that of CH_4, the addition of CO_2 to the fuel reduces the adiabatic temperature, due to the aforementioned heat capacity of carbon dioxide. This means a share of the energy will be spent by the CO_2, having the same effect as a heat loss.

As mentioned, the main mechanism for NO_x generation under lean and stoichiometric conditions is thermal, and pollutant levels share the same trend as the adiabatic temperature, and follow the slight increase for the fuels with a greater fraction of hydrogen. However, for the rich conditions, the dominating mechanism becomes the prompt NO_x formation, which explains the slight drop as temperature drops after stoichiometry, and the subsequent rise as ϕ rises.

For low NO_x LSB operation, lean conditions are always desired, as the effect of the prompt mechanism becomes minimal, and the effect of the thermal mechanism is heavily reduced. Adiabatic results show low levels of NO_x of about 20 ppm, or less for the biogas based fuels, showing a sharp reduction under the leaner conditions. Results showed that neither the addition of hydrogen nor biogas increased the emissions levels considerably. While the addition of hydrogen increases the emission levels slightly, the effect is very small and the emissions can be reduced by burning under leaner conditions, taking advantage of the increased flame stability of hydrogen blends. Biogas, on the other hand, reduces the levels of pollutants when compared to equivalent methane flames. This is due to the absorption of energy by the CO_2, causing the flame temperature to decrease and a smaller effect of thermal NO_x generation. If these results are taken into account with the results of Section 4.3, showing a possibility of stabilizing flames for equivalence ratios as low as 0.5 by adding hydrogen, a very good case can be made for the very low NO_x claim of previous studies for the LSB [14, 22].

Chapter 5

Conclusions

This work was divided into three main objectives. The first one was to confirm the feasibility of an LSB burner, 2.54 cm in diameter, in the laboratory. For this, a setup was assembled and PIV images were obtained for a range (20 V to 140 V) of ventilator velocities. From these, the typical LSB flow field was observed, both in a plane normal to the burner exit and a plane parallel to it. The non-dimensional ratio used to define swirl burners was also calculated from these measurements (an average of 0.5), and was found to be within the low-swirl operating interval.

The second objective was to evaluate the effects of using biogas as a fuel, and enriching it with hydrogen. A set of conditions was established, defining a pure methane mixture and two levels of carbon dioxide addition, a mixture of 80% CH_4 and 20% CO_2, and a mixture of 60% CH_4 and 40% CO_2. The effect of the addition of each species was then analysed in two different ways. Firstly, the flame properties for three different equivalence ratios ($\phi = 0.9$, $\phi = 1$ and $\phi = 1.2$) were assessed by compiling a set of 140 images of the flame, comparing the behaviour for all different conditions using a direct pictures of the flame and three types of bandwidth filters from where the formation within the flame of three species (C_2, CH and CO_2) was analysed. These results were then processed to obtain a brightness based outline of the flame, helping evaluate such parameters as flame shape and position. Results showed that the increase of the fraction of carbon dioxide in the biogas mixture causes the flame to become less bright, to anchor in a position further downstream and to have a more elongated, narrow shape. This is a result of the properties of CO_2 as an inert gas, diluting the properties of methane and reducing parameters such as flame speed S_L and heat release rate. The addition of hydrogen, on the other hand, had the opposite effect on the flames, causing generally shorter, wider and more intense flames than the ones with no hydrogen content. The flames also stabilized in a position further upstream, which can be attributed to the increased flame speed and higher heat release rate of H_2. These effects of hydrogen addition were more noticeable in the flames with higher levels of CO_2. The LSB was also able to hold the flame in the transient conditions between the set points, meaning the fuel composition can be quickly and effortlessly changed.

Flame limits were then studied to evaluate the adaptability of the LSB design to the fuel conditions. Each of the previously mentioned fuel conditions was set, and the air flow rate was varied until blow-off

was observed to determine the lean limit for each composition. The flashback limits were not defined, as the LSB combustion focuses on lean combustion, making the lean limits much more relevant. Again, it was observed that the addition of CO_2 was detrimental to the flame properties, and it caused the lean limit of methane flames to rise significantly. However, hydrogen was proved to substantially improve the lean stability of the flames, especially for fuels with more CO_2, partly dissimulating the negative effects of carbon dioxide.

Lastly, simulations were made for the same conditions using the GRI Mech 3.0 mechanism, with the goal of obtaining a trend for the effects of fuel composition on the emissions of NO_x. The overall trend of results for ϕ was consistent with the expected results considering the NO_x formation mechanisms. Higher fractions of carbon dioxide were shown to reduce NO_x levels, while hydrogen addition was shown not to have a significant impact on NO_x formation, increasing it only slightly when compared to pure methane and biogas flames, especially around stoichiometry. This can again be traced to the inert nature of CO_2, which, together with its high specific heat, causes the flame temperature to drop, consequently causing thermal NO_x formation to decrease, while the adiabatic temperature of hydrogen is only marginally higher than that of methane, meaning thermal NO_x formation does not increase considerably. These results also set a very positive tendency for very low NO_x levels in leaner regimes ($\phi < 0.8$), validating the LSB design as a low-NO_x technology.

5.1 Future Work

Although the development of this work has achieved a good level of understanding on the adaptability of low-swirl burners, it has led to several possibilities for future research on this topic:

1. The LSB reacting flow field is affected by the thermal impact of the flame on the flow, accelerating it and possibly changing the flow field and flame structure. Therefore, a reacting PIV analysis could provide an insight on this possibility;

2. Although the emission levels simulations showed promising results for lean flames, a study on the emissions of the LSB, particularly at lean conditions, could confirm the low NO_x claim.

3. The conditions of this study were, when compared to most studies on LSB, low power output, low Reynolds conditions. There are few studies on such small LSB applications, and the effects of burner size reduction are not well defined. Thus, a study with a diameter variation, possibly reducing it, could open possibilities for low power output applications.

Bibliography

[1] I. E. Agency. World energy investment, 2019. URL `https://www.iea.org/reports/world-energy-investment-2019/energy-end-use-and-efficiency`.

[2] M. Kampa and E. Castanas. Human health effects of air pollution. *Environmental Pollution*, 151: 362–367, 2008.

[3] E. E. Agency. European union emission inventory report, 2017.

[4] G. Esposito, L. Frunzo, A. Giordano, F. Liotta, A. Panico, and F. Pirozzi. Anaerobic co-digestion of organic wastes. *Reviews in Environmentsl Science and Bio/Technology*, 11:325–341, 2012.

[5] R. Kadam and N. L. Padwar. Recent advancement in biogas enrichment and its applications. *Renewable and Sustainable Energy Reviews*, 73:892–903, 2017.

[6] L. Pizzuti, C. A. Martins, and P. T. Lacava. Laminar burning velocity and flammability limits in biogas: A literature review. *Renewable and sustainable Energy Reviews*, 62:856–865, 2016.

[7] Z. Hu and X. Zhang. Experimental study on flame stability of biogas/hydrogen combustion. *International Journal of Hydrogen Energy*, 44:5607–5614, 2019.

[8] M. C. Drake and R. J. Blint. Calculations of nox formation pathways in propagating laminar, high pressure premixed ch4/air flames. *Combustion Science and Technology*, 75:261–285, 1991.

[9] N. Syred and J. M. Beér. Combustion in swirling flows: A review. *Combustion and Flame*, 23: 143–201, 1974.

[10] D. G. Lilley. Swirl flows in combustion: A review. *AIAA Journal*, 15(8):1063–1077, 1977.

[11] C. K. Chan, K. S. Lau, W. K. Chin, and R. K. Cheng. Freely propagating open premixed turbulent flames stabilized by swirl. *Symposium (International) on Combustion*, 24(1):511–518, 1992.

[12] D. T. Yegian and R. K. Cheng. Development of a vane-swirler for use in a low no_x weak-swirl burner. 10 1996. doi: 10.2172/414339.

[13] P. Therkelsen, D. Littlejohn, and R. K. Cheng. Parametric study of low-swirl injector geometry on its operability. *Proc. of ASME Turbo Expo 2012*, pages 309–318, 2012.

[14] R. K. Cheng, D. Littlejohn, W. A. Nazeer, and K. O. Smith. Laboratory studies of the flow field characteristics of low-swirl injectors for adaptation to fuel-flexible turbines. *Journal of Engineering for Gas Turbines and Power*, 130:021501 1–10, 2008.

[15] D. Beerer, V. McDonell, R. K. Cheng, and P. Therkelsen. Flashback, blow out, emissions, and turbulent displacement flame speed measurements in a hydrogen and methane fires low-swirl injector at elevated pressures and temperatures. *Proc. of ASME Turbo Expo 2012*, 2012.

[16] A. Frank, P. Therkelsen, M. S. Aznar, V. H. Rapp, R. K. Cheng, and J. Y. Chen. Investigation of the down-scaling effects on the low swirl burner and its application to microturbines. *Proc. of ASME Turbo Expo 2018: Turbomachinery Technical Conference and Exposition*, GT2018–77208, 2018.

[17] D. Littlejohn, R. K. Cheng, D. R. Noble, and T. Lieuwen. Laboratory investigations of low-swirl injectors operating with syngases. *Journal of Engineering for Gas Turbines and Power*, 132:011502 1–8, 2010.

[18] N. A. Chigier and J. M. Beér. Velocity and static-pressure distributions in swirling air jets issuing from annular and divergent nozzles. *Journal of Basic Engineering*, 23:788–796, 1964.

[19] H. J. Sheen, W. J. Chen, S. Y. Jeng, and T. L. Huang. Correlation of swirl number for a radial-type swirl generator. *Experimental Thermal and Fluid Science*, 12:444–451, 1996.

[20] C. J. Lawn. *Principles of combustion engineering for boilers*. Academic Press, 7^{th} edition edition, 1987. ISBN 978–0–12–439035–5.

[21] T. Plessing, C. Kortschik, N. Peters, M. S. Mansour, and R. K. Cheng. Measurements of the turbulent burning velocity and the structure of premixed flames on a low-swirl burner. *Proc. of the Combustion Institute*, 28:359–366, 2000.

[22] D. Littlejohn and R. K. Cheng. Fuel effects on a low-swirl injector for lean premixed gas turbines. *Proc. of the Combustion Institute*, 31:3155–3162, 2007.

[23] R. K. Cheng, D. Littlejohn, P. A. Strakey, and T. Sidwell. Laboratory investigations of a low-swirl injector with h_2 and ch_4 at gas turbine conditions. *Proc. of the Combustion Institute*, 32:3001–3009, 2009.

[24] M. R. Johnson, D. Littlejohn, W. A. Nazeer, K. O. Smith, and C. R. K. A comparison of the flowfields and emissions of high-swirl injectors and low-swirl injectors for lean premixed gas turbines. *Proc. of the Combustion Institute*, 30:2867–2874, 2005.

[25] F. Quintino and E. Fernandes. Analytical correlation to model diluent concentration repercussions on the burning velocity of biogas lean flames: Effect of co2 and n2. *Biomass and bioenergy*, 119: 354–363, 2018.

[26] C. D. Rakopoulos and C. N. Michos. Generation of combustion irreversibilities in a spark ignition engine under biogas–hydrogen mixtures fueling. *International Journal of Hydrogen Energy*, 34:4422–4437, 2009.

[27] S. R. Turns. *An Introduction to Combustion*. McGraw-Hill, 3rd edition edition, 2011. ISBN 978–0–07–338019–3.

[28] C. Dong, Q. Zhou, X. Zhang, Q. Zhao, T. Xu, and S. Hui. Experimental study on the laminar flame speed of hydrogen/natural gas/air mixtures. *Frontiers of Chemical Engineering in China*, 4:417–422, 2010.

[29] F. M. White. *Fluid Mechanics*. McGraw-Hill, 7th edition edition, 2011. ISBN 978–0–07–352934–9.

[30] A. A. Verbeek, T. W. F. M. Bouten, G. G. M. Stoffels, B. J. Geurts, and T. H. van der Meer. Fractal turbulence enhancing low-swirl combustion. *Combustion and Flame*, 162:129–143, 2015.

[31] M. E. Feyz, J. A. Esfahani, I. Pishbin, and S. M. R. Modarres Razavi. Effect of recess length on the flame parameters and combustion performance of a low swirl burner. *Applied Thermal Engineering*, 89:609–617, 2015.

[32] D. G. Goodwin, R. L. Speth, H. K. Moffat, and B. W. Weber. Cantera: An object-oriented software toolkit for chemical kinetics, thermodynamics, and transport processes, 2018. URL `https://zenodo.org/record/1174508#.X2CskD-S1PY`.

[33] G. P. Smith, D. M. Golden, M. Frenklach, N. W. Moriarty, B. Eiteneer, M. Goldenberg, C. Thomas Bowman, R. K. Hanson, S. Song, W. C. Gardiner Jr., V. V. Lissianski, and Z. Qin. Grimech 3.0. URL `http://www.me.berkeley.edu/gri_mech/`.

[34] F. Quintino, T. P. Trindade, and E. Fernandes. Biogas combustion: Chemiluminescence fingerprint. *Fuel*, 231:328–340, 2018.

[35] C. Ji, D. Wang, J. Yang, and S. Wang. A comprehensive study of light hydrocarbon mechanisms performance in predicting methane/hydrogen/air laminar burning velocities. *International Journal of Hydrogen Energy*, 42:17260–17274, 2017.

[36] A. A. Konnov, A. Mohammad, R. K. Velamati, N. I. Kim, C. Prathap, and S. Kumar. A comprehensive review of measurements and data analysis of laminar burning velocities for various fuel + air mixtures. *Progress in Energy and Combustion Science*, 68:197–267, 2018.

[37] M. Salcudean, D. C. Groeneveld, and L. Leung. Effect of flow-obstruction geometry on pressure drops in horizontal air-water flow. *International Journal of Multiphase Flow*, 9:73–85, 1983.

[38] H. Zhen, C. W. Leung, C. Cheung, and Z. H. Huang. Combustion characteristic and heating performance of stoichiometric biogas-hydrogen-air flame. *International Journal of Heat and Mass Transfer*, 92:807–814, 2016.

[39] M. Day, S. Tachibana, J. Bell, M. Lijewski, V. Beckner, and R. K. Cheng. A combined computational and experimental characterization of lean premixed turbulent low swirl laboratory flames i. methane flames. *Combustion and Flame*, 159:275–290, 2012.

[40] M. Day, S. Tachibana, J. Bell, M. Lijewski, V. Beckner, and R. K. Cheng. A combined computational and experimental characterization of lean premixed turbulent low swirl laboratory flames ii. hydrogen flames. *Combustion and Flame*, 162:2148–2165, 2015.

Appendix A

Flame Images

Filtered and unfiltered flames for $\phi = 0.9; 1; 1.2$. Top Row: Methane; Middle Row: 80/20 Biogas; Bottom Row: 60/40 Biogas. Left to Right: 0, 10, 20, 30% H_2.

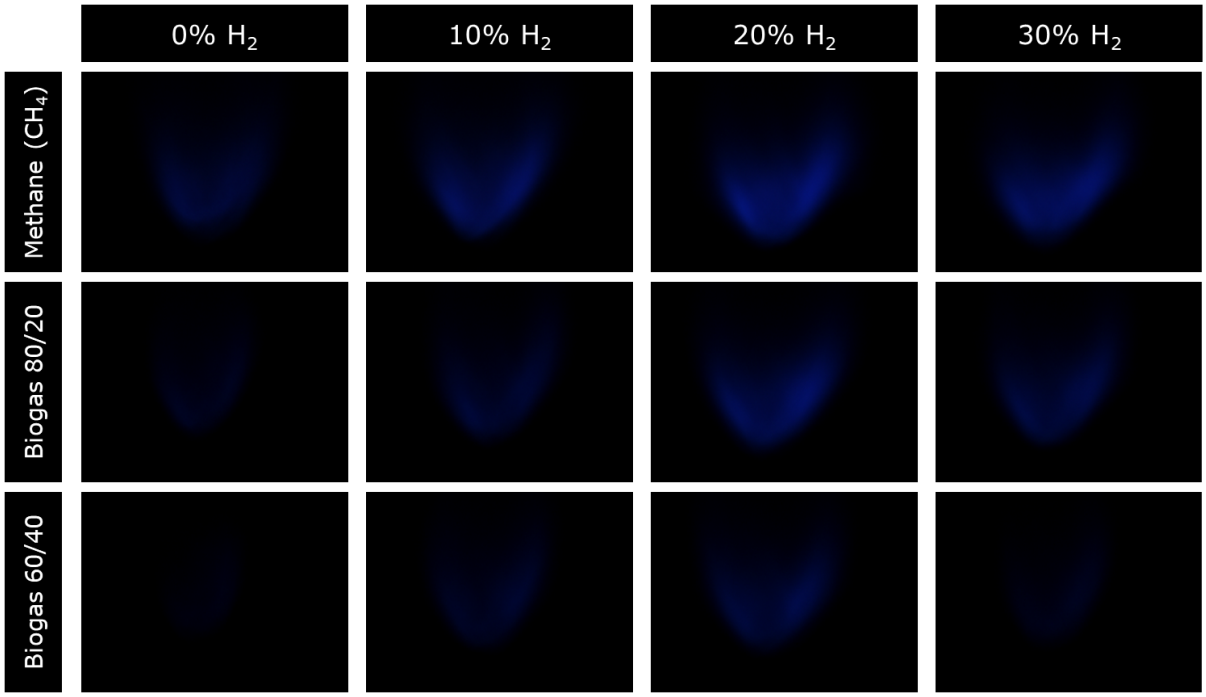

Figure A.1: Unfiltered flames for $\phi = 0.9$.

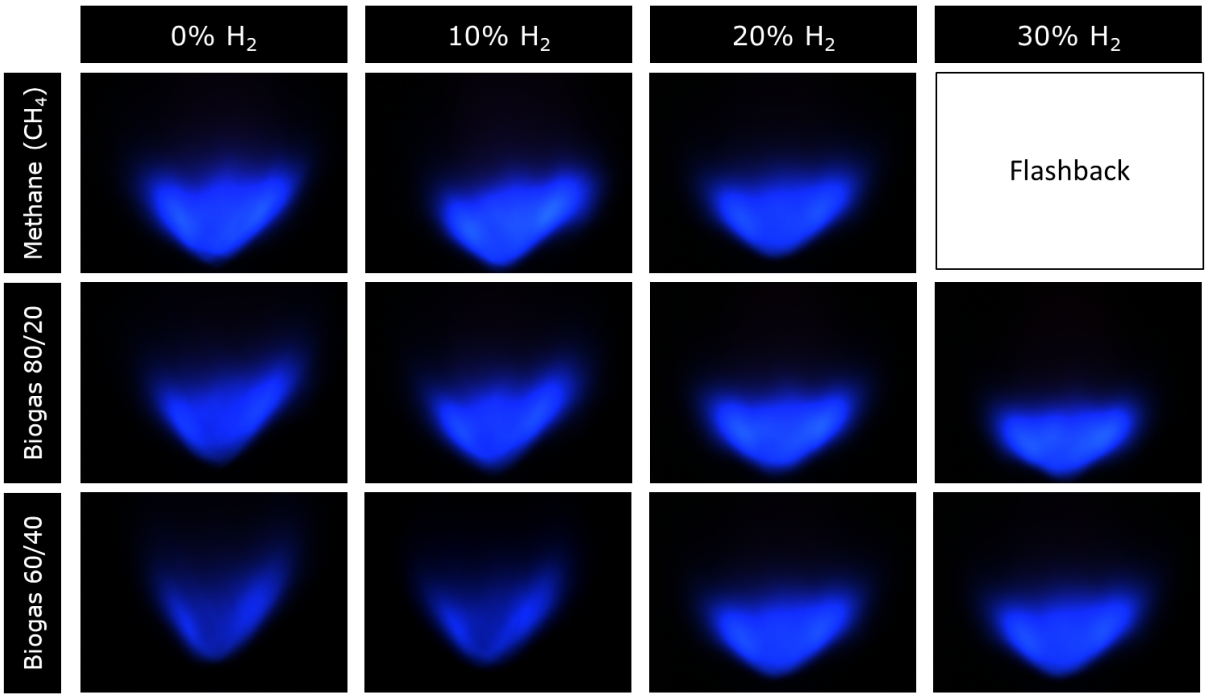

Figure A.2: Unfiltered flames for $\phi = 1.2$.

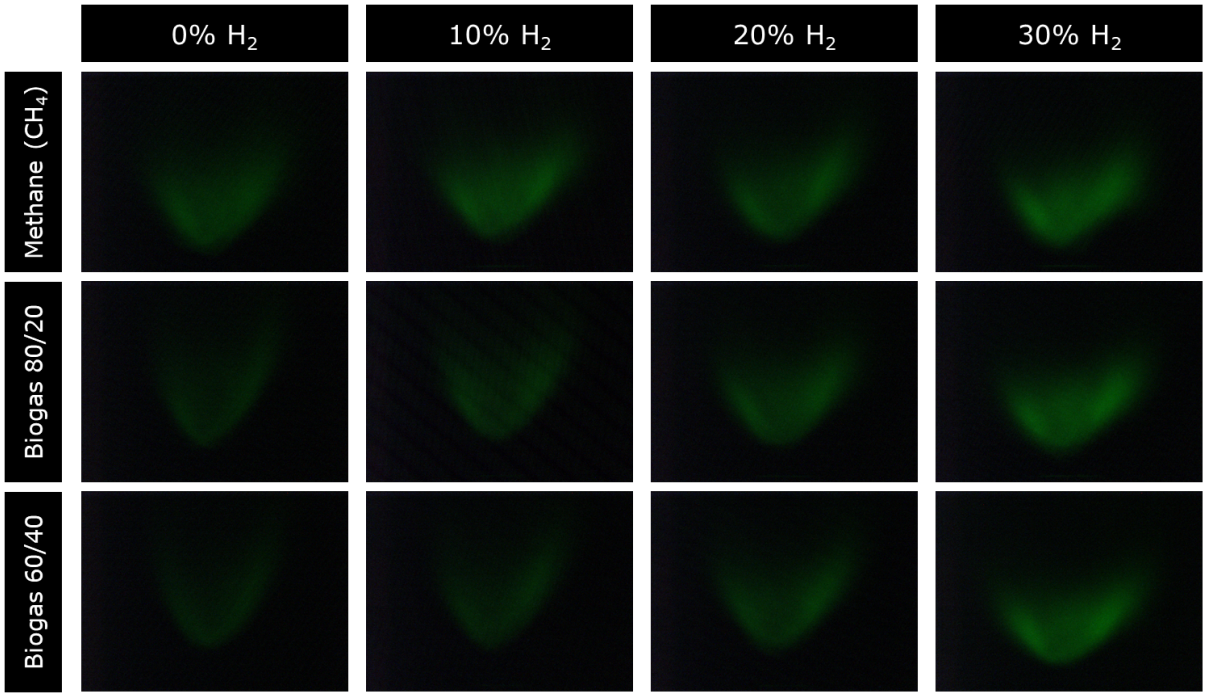

Figure A.3: Filtered flames for $\phi = 1$, λ =516nm bandpass filter for C_2.

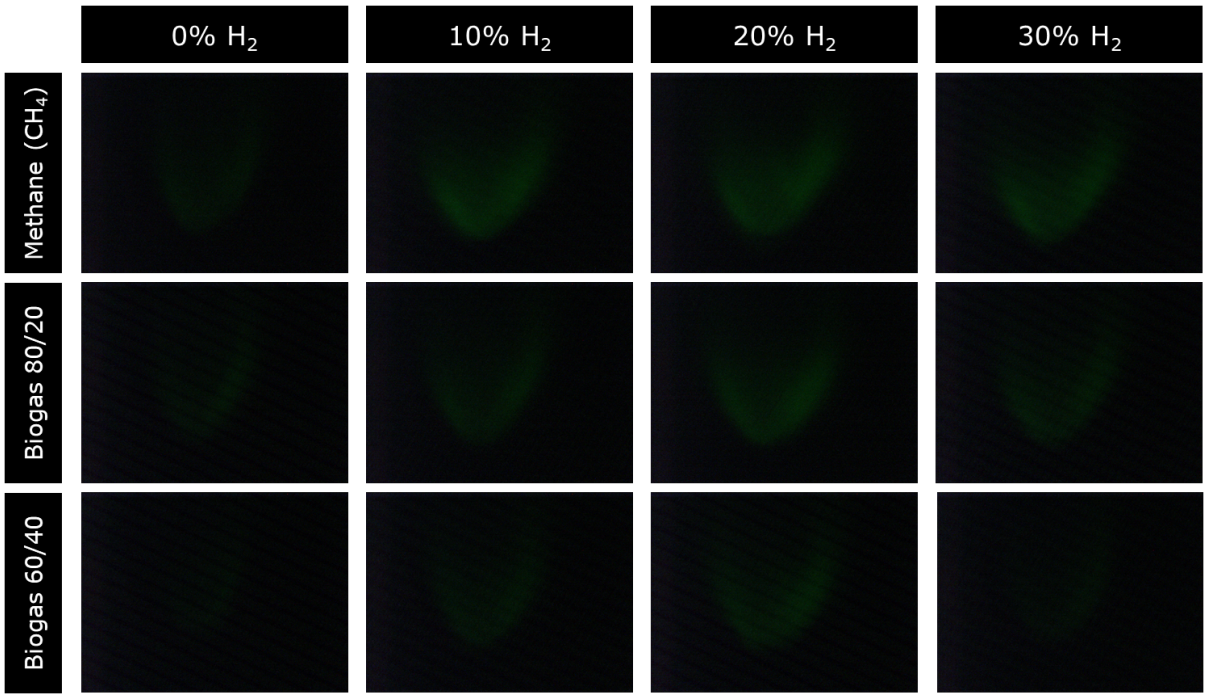

Figure A.4: Filtered flames for $\phi = 0.9$, λ =516nm bandpass filter for C_2.

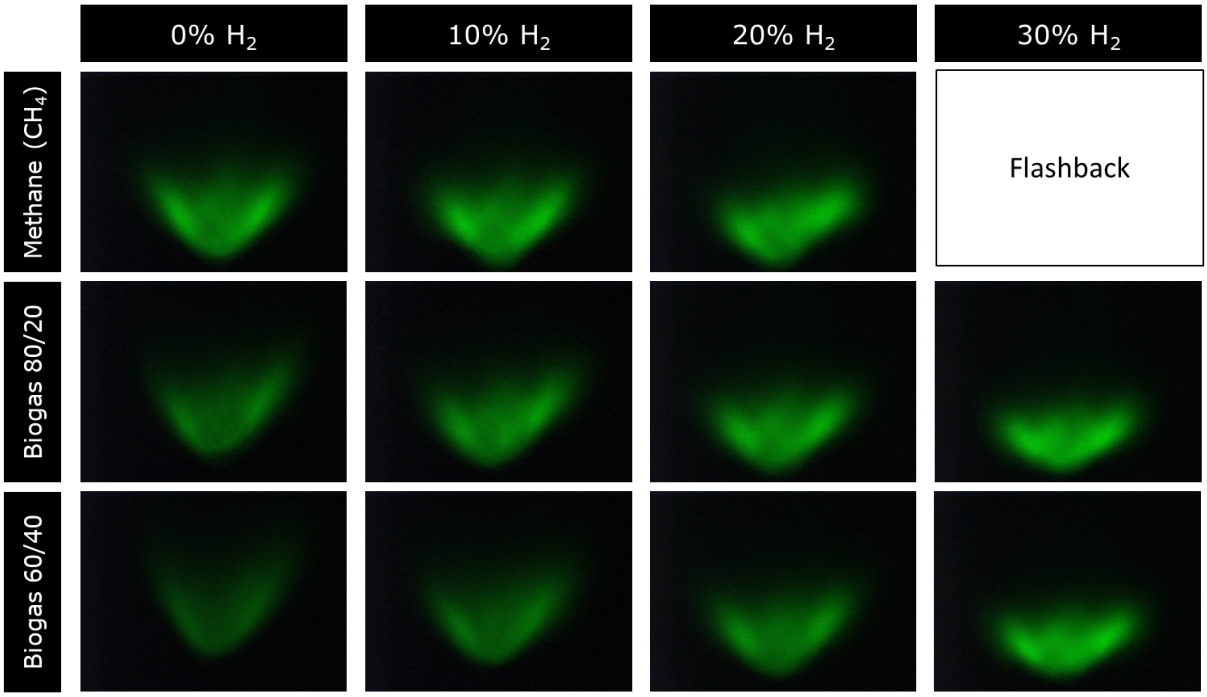

Figure A.5: Filtered flames for $\phi = 1.2$. λ =516nm bandpass filter for C_2.

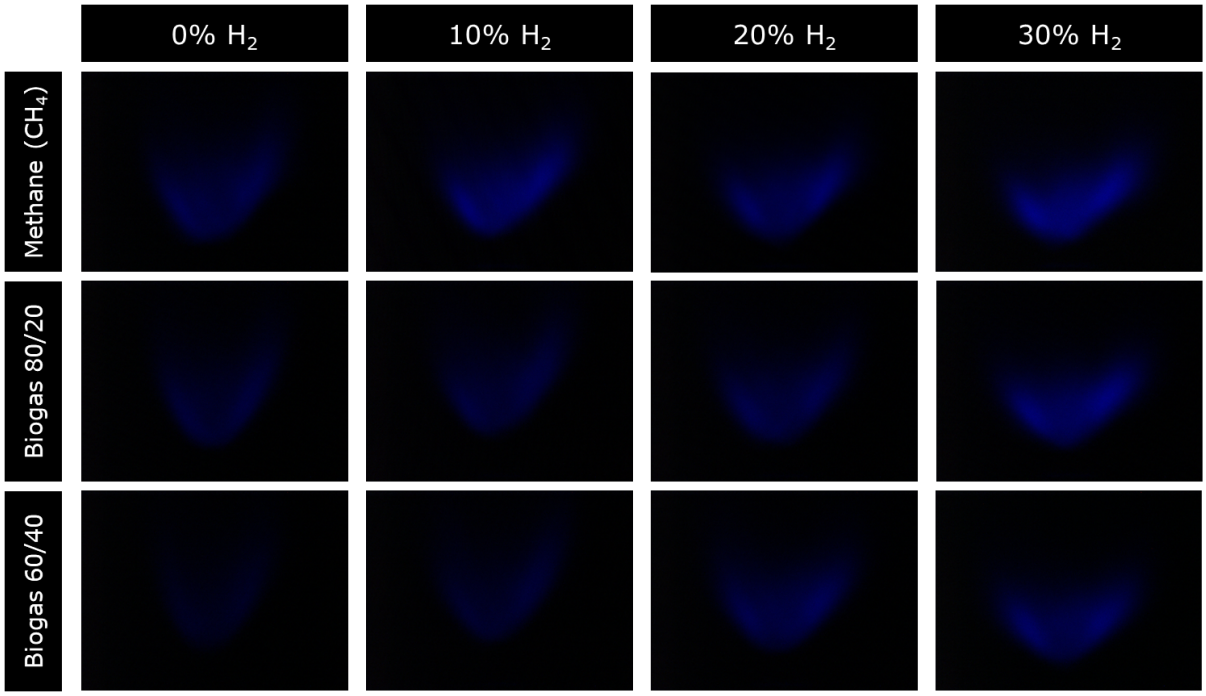

Figure A.6: Filtered flames for $\phi = 1$, λ =431nm bandpass filter for CH.

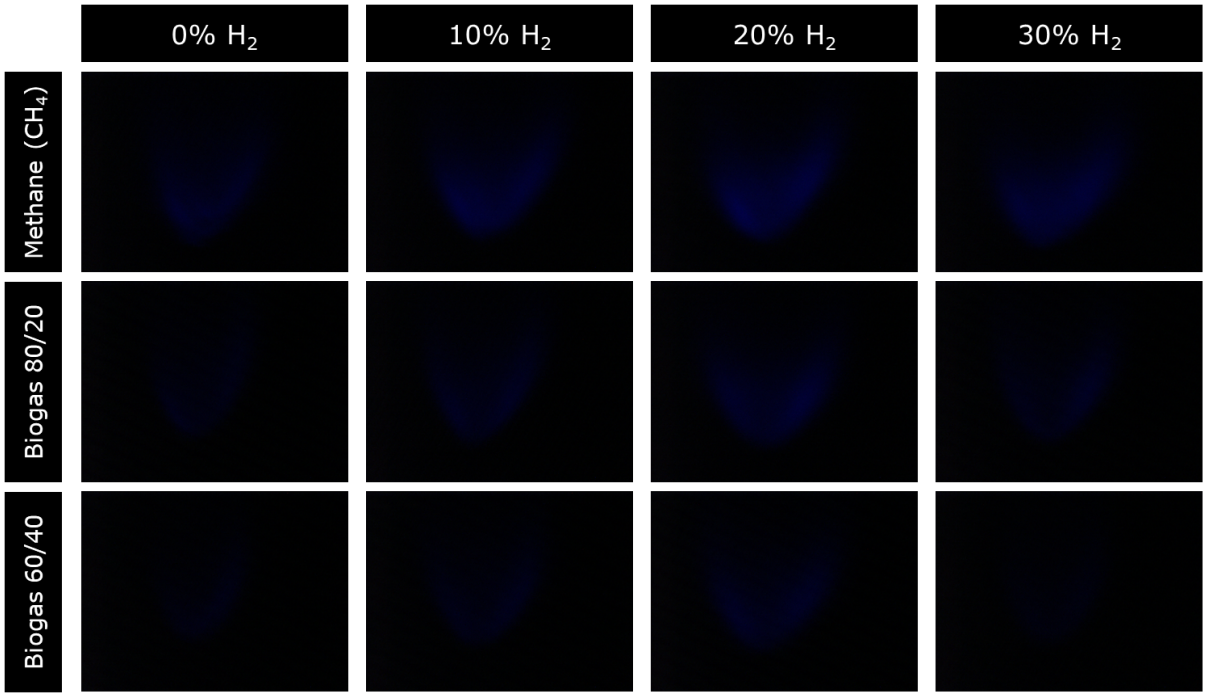

Figure A.7: Filtered flames for $\phi = 0.9$, λ =431nm bandpass filter for CH.

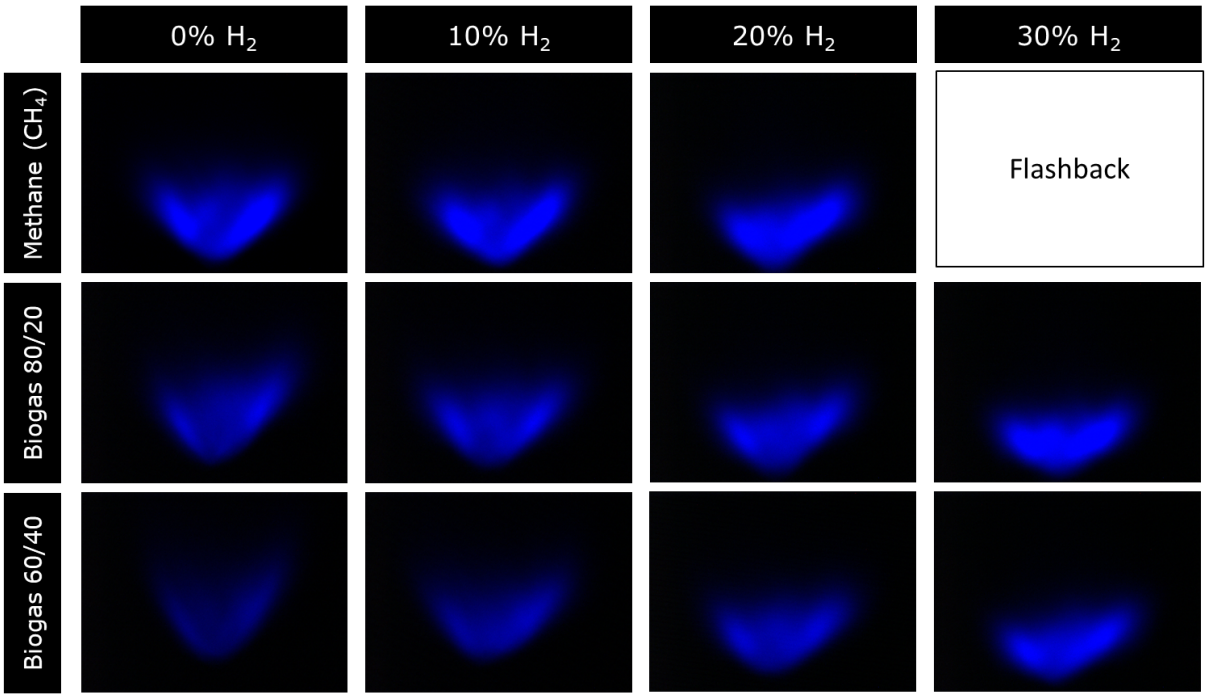

Figure A.8: Filtered flames for $\phi = 1.2$. λ =431nm bandpass filter for CH.

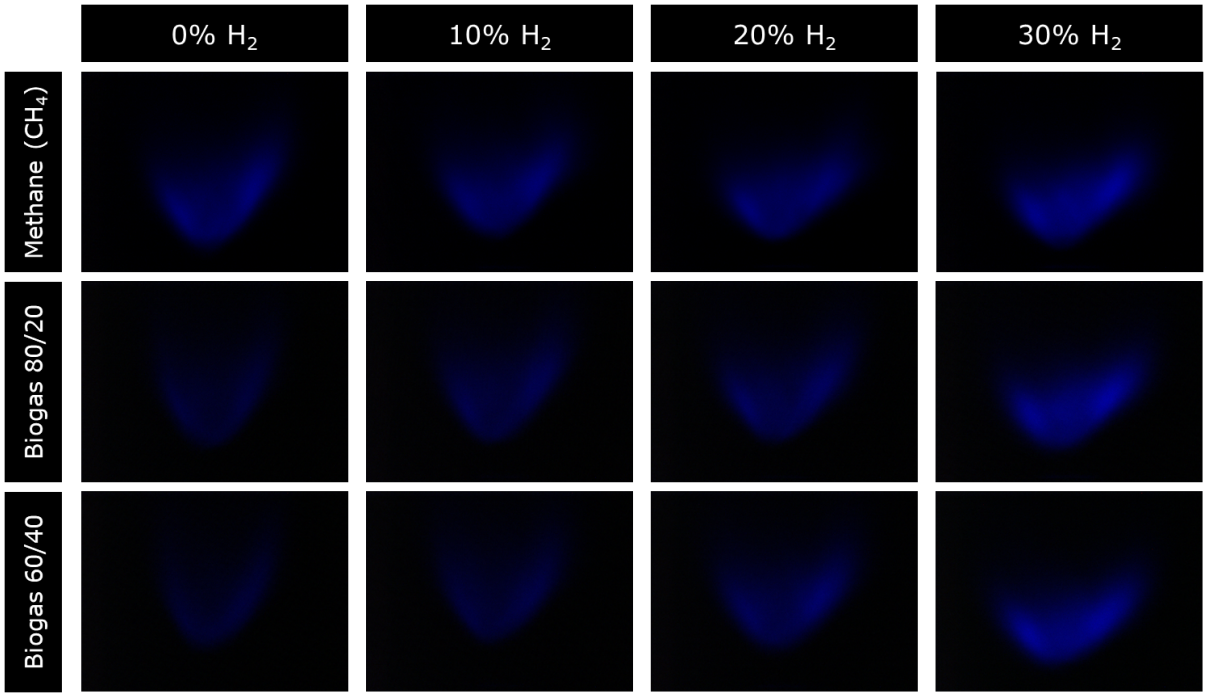

Figure A.9: Filtered flames for $\phi = 1$, λ =451nm bandpass filter for CO_2.

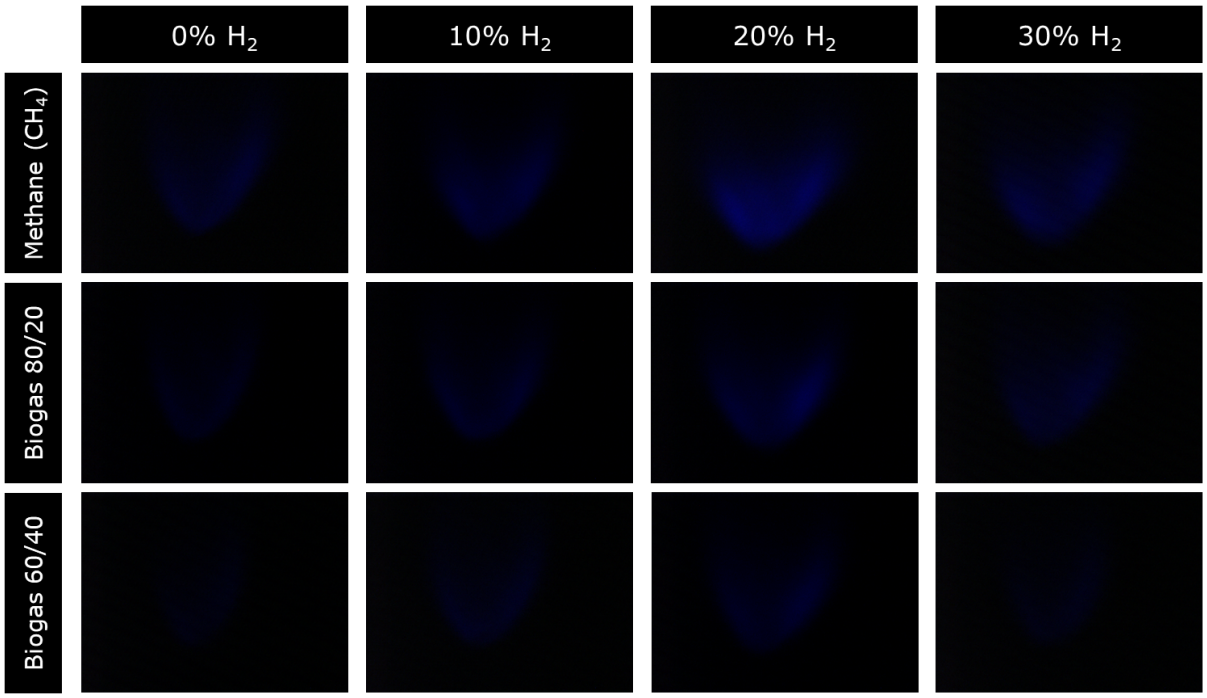

Figure A.10: Filtered flames for $\phi = 0.9$, λ =451nm bandpass filter for CO_2.

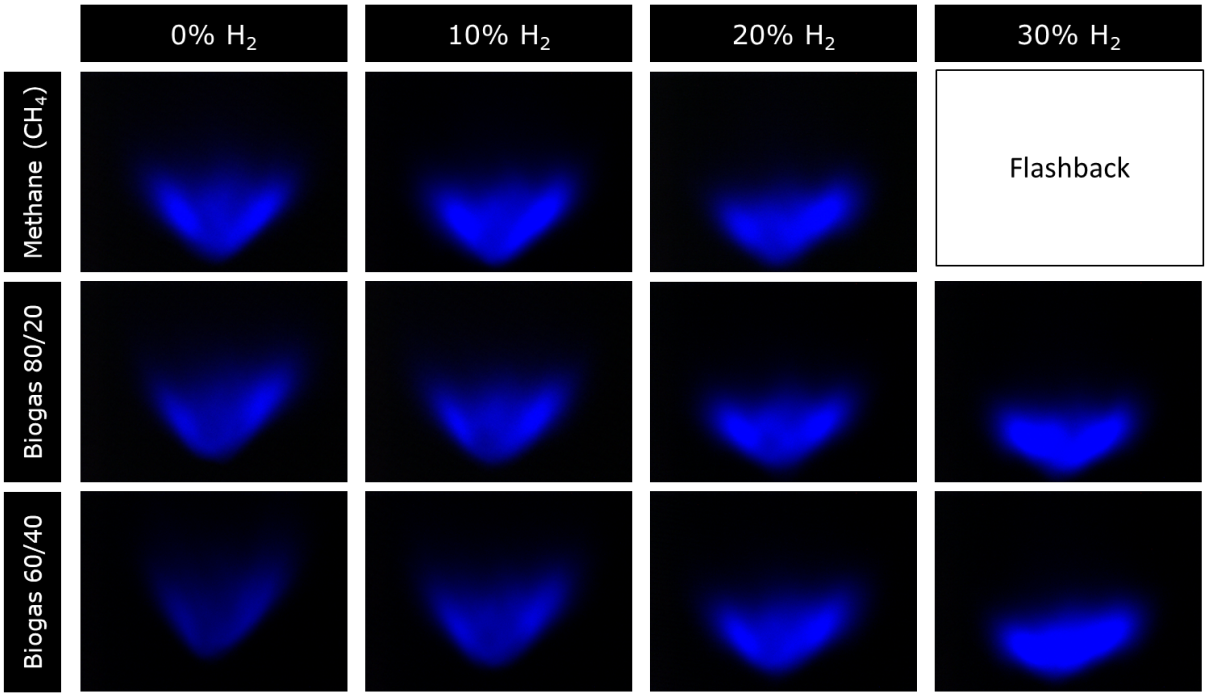

Figure A.11: Filtered flames for $\phi = 1.2$. λ =451nm bandpass filter for CO_2.